Multilinear modeling and controller design for a plate heat exchanger of a PEM electrolyzer

A Thesis Presented for
the Degree of Master of Science in
Renewable Energy Systems

by

Nícolas Miranda Hernández

Matriculation number: [redacted]

Submission date: 24.06.2024

Hamburg University of Applied Sciences
Faculty of Life Sciences

First examiner:
Prof. Dr. Gerwald Lichtenberg

Fraunhofer Institute for Wind Energy Systems
Application Center for Integration of
Local Energy Systems

Second examiner:
Dr.-Ing. Georg Pangalos

Supervisor:
MSc. Aline Luxa

Statutory declaration

By:	Miranda Hernández, Nícolas
Matriculation number:	[redacted]

Statutory declaration I hereby confirm that I have prepared this Master's thesis independently and without external assistance, that I have only used the sources and materials indicated, and that all quotations from other works have been identified as such and properly acknowledged in the thesis.

(Date) (Signature)

Abstract

The increasing share of renewable energy (RE) in the German electricity grid has led to the curtailment of RE plants due to potential risks to the existing transmission infrastructure caused by the intermittent nature of RE. To address this issue, the production of green hydrogen through proton exchange membrane water electrolysis (PEMWE) systems has emerged as a vital solution, serving as a chemical energy storage and grid operation support to prevent the curtailment of RE plants. To ensure the long-term reliable operation of these electrolysis assets, temperature control of the feed water for electrolysis is of vital importance. This thesis focuses on the practical design of a plate heat exchanger (PHE) and a PID controller for controlling the feed water temperature of a proton exchange membrane (PEM) electrolyzer. The research involved developing a tailored PHE model for the cooling system of a 1 MW PEM electrolyzer and investigating its first principles (FP), linear time-invariant (LTI), and multilinear time-invariant (MTI) modeling approaches. The designed PHE coupled the electrolyzer's feed water with the cooling water pumped circuits, enabling control of the electrolyzer's feed water temperature using a PID controller to adjust the flow rate of the cooling water pump. The results show that the PHE MTI model accurately captures the dynamics of the FP model, consistently outperforming the LTI model. Furthermore, the PHE MTI model exhibits a 74 % reduction in simulation time compared to the FP model for this application. Suitable PID controller parameters were identified for effective feed water temperature control. Leveraging the structure of the electrolyzer's cooling system model developed, an assessment of power consumption in the balance of plant (BOP) components associated with the electrolyzer's cooling system is conducted. This assessment aids in gaining a comprehensive understanding of energy consumption patterns in the electrolyzer, a crucial step toward optimizing power usage in BOP components. The estimation and breakdown of power consumption associated with the variable flow rate in the cooling water pump and the constant flow rate in the feed water pump reveal that the feed water pump accounts, on average, for 97 % of the power consumption in the cooling system. Overall, the consumption related to operating the electrolyzer's cooling system represents 1 % to 5.4 % of the total power consumption of the electrolyzer. This thesis provides a solid framework for analyzing and modeling thermal dynamics and power consumption patterns in PEM electrolyzers' cooling systems. It can be used as a basis for further research on optimizing power usage in BOP components, implementing advanced control strategies for feed water temperature regulation, and modeling of PHEs.

Contents

List of Tables ix

List of Figures x

List of Abbreviations xii

List of Symbols xv

1 Introduction 1

1.1 Motivation . . . 2
1.2 Aim of the thesis . . . 2
1.3 Structure of the thesis . . . 3

2 Fundamentals 4

2.1 Proton exchange membrane water electrolyzers . . . 4
2.2 Heat transfer theory . . . 7
2.2.1 Energy balances . . . 7
2.2.2 Heat transfer relationships . . . 8
2.2.3 Thermal methods for heat exchangers . . . 9
2.3 Plate heat exchangers (PHEs) . . . 12
2.3.1 Configuration and assembly . . . 12
2.3.2 Thermal and hydraulic correlations . . . 13
2.3.3 Sizing . . . 15
2.4 Estimation of thermodynamic properties . . . 17
2.5 State space models . . . 19
2.5.1 Linear time-invariant (LTI) models . . . 19
2.5.2 Multilinear time-invariant (MTI) models . . . 20
2.6 PID control . . . 21
2.7 Power consumption of pumps . . . 22
2.7.1 Pressure drop in round pipes . . . 23
2.7.2 Pressure drop in PHE . . . 24
2.7.3 Pressure drop in other equipment . . . 25

3 Model definitions and structure 27
3.1 Electrolyzer base model . . . 27
3.2 Electrolyzer updated model . . . 29
3.3 PHE sizing and first principles (FP) modeling . . . 31
3.4 PHE modeling approaches . . . 32
3.4.1 LTI modeling . . . 33
3.4.2 MTI modeling . . . 33
3.5 PID Controller . . . 34
3.6 Estimation of pump power consumption . . . 35
3.6.1 Pressure drop in piping network . . . 35
3.6.2 Pressure drop in other equipment . . . 36

4 Simulation results and discussion 37
4.1 PHE sizing . . . 37
4.2 PHE models comparison . . . 38
4.3 PID controller perfomance . . . 40
4.3.1 Plant with PHE FP model . . . 41
4.3.2 Plant with PHE MTI model . . . 43
4.4 Pumps power consumption . . . 46

5 Conclusion 49
5.1 Summary . . . 49
5.2 Outlook . . . 50

Bibliography I

A Appendix VII
A.1 Fluid properties sensitivity analysis . . . VII

List of Tables

Table 2.1 Single-phase heat transfer correlation parameters for PHE 16
Table 2.2 Fundamental and critical properties of pure water 17
Table 2.3 Liquid density estimation parameters 18
Table 2.4 Liquid dynamic viscosity estimation parameters 18
Table 2.5 Liquid thermal conductivity estimation parameters 18
Table 2.6 Liquid specific heat capacity estimation parameters 19

Table 3.1 Parameters of 1 MW electrolyzer base model 28
Table 3.2 Parameters of 1 MW electrolyzer updated model 29
Table 3.3 PHE plates characteristics 32
Table 3.4 Container dimensions for 1 MW electrolyzer 35
Table 3.5 Pipe routing geometry 36

Table 4.1 PHE properties and thermal performance indicators 37
Table 4.2 Stream properties for PHE sizing 38
Table 4.3 Controllers tested in electrolyzer model 40
Table 4.4 Set up and performance parameters of Controller 1 41
Table 4.5 Set up and performance parameters of Controller 2 43
Table 4.6 Set up and performance parameters of Controller 3 44
Table 4.7 Set up and performance parameters of Controller 4 45
Table 4.8 PID controllers performance comparison 46
Table 4.9 Pressure drop summary for fluid circuits 47

Table A.1 Sensitivity analysis of selected fluid properties VII
Table A.2 Steady-state condition of reference case of study VIII
Table A.3 Average fluid properties calculated for reference case of study IX
Table A.4 Calculated error for PHE outlet temperatures IX

List of Figures

Figure 2.1 Proton exchange membrane water electrolysis (PEMWE) cell 5
Figure 2.2 Polarization curve of an electrolysis cell 6
Figure 2.3 Block diagram of a PEMWE system 6
Figure 2.4 Feed water cooling system of a PEM electrolyzer 7
Figure 2.5 Heat transfer across a conductive plate 8
Figure 2.6 Thermal resistances across a conductive plate 9
Figure 2.7 Relationship ε-NTU for counterflow 12
Figure 2.8 Gastketed PHE layout 13
Figure 2.9 Plate patterns for PHE 13
Figure 2.10 Gasketed PHE with single U-pass arrangement 14
Figure 2.11 Main dimensions of a chevron plate 15
Figure 2.12 Counter-flow PHE schematic. 15
Figure 2.13 NTU interval for PHE design. 17
Figure 2.14 System with input, output and state 19
Figure 2.15 Feedback PID control 22
Figure 2.16 Fluid energy levels in pumping circuit 23

Figure 3.1 Structure of the 1 MW electrolyzer base model 28
Figure 3.2 Structure of the 1 MW electrolyzer updated model 30
Figure 3.3 Target performance parameters in the MATLAB PID Tuner App . . . 35

Figure 4.1 Thermal performance of the sized PHE 38
Figure 4.2 PHE models performance at design case scenario. 38
Figure 4.3 PHE models performance with variable cold fluid flow 39
Figure 4.4 PHE FP and MTI model performance at low cold fluid low 40
Figure 4.5 Stack power input curve. 41
Figure 4.6 Electrolyzer behavior with PHE FP model and PID Controller 1 42
Figure 4.7 PHE temperature crossed profiles 43
Figure 4.8 Electrolyzer's behavior with PHE MTI model and PID Controller 2 . . 44
Figure 4.9 Electrolyzer's behavior with PHE MTI model and PID Controller 3 . . 45
Figure 4.10 Volume flow profiles of hot and cold fluid 47
Figure 4.11 Pumps power consumption profiles 48

Figure 4.12 Pumps power consumption allocation 48

Figure A.1 Sensitivity analysis of fluid properties VIII

List of Abbreviations

BOP balance of plant

CP canonical polyadic

EoL end of life

FP first principles

GHG greenhouse gas

HE heat exchanger

LMTD logarithmic mean temperature difference

LTI linear time-invariant

MPC model predictive control

MTI multilinear time-invariant

NTU number of transfer units

PEM proton exchange membrane

PEMWE proton exchange membrane water electrolysis

PG38 % propylene glycol 38 %

PHE plate heat exchanger

RE renewable energy

RMSE root-mean-square error

List of Symbols

Symbol	Definition	Unit
A	heat transfer area	m^2
b	mean mass channel gap	m
C	heat capacity rate	$\mathrm{W\,K}^{-1}$
C_{ch}	PHE channel constant	
c_p	heat capacity	$\mathrm{J\,kg}^{-1}\,\mathrm{K}^{-1}$
d	diameter	mm
F_c	complexity factor for piping	
f	friction factor	
G	mass velocity	$\mathrm{kg\,m}^{-2}\mathrm{s}^{-1}$
h	heat transfer coefficient	$\mathrm{W\,m}^{-2}\,\mathrm{K}^{-1}$
i	electric current density	$\mathrm{A\,cm}^{-2}$
K_d	PID controller derivative term	
K_i	PID controller integral term	
K_p	PID controller proportional term	
k	thermal conductivity	$\mathrm{W\,m}^{-1}\,\mathrm{K}^{-1}$
L	length or distance	m
$\dot{m}$	mass flow	$\mathrm{kg\,s}^{-1}$
$\dot{n}$	molar flow	$\mathrm{mol\,s}^{-1}$
n	number of (see corresponding script)	
P	power	kW
p	pressure	kPa
$\Delta\hat{p}_{\mathrm{pipe}}$	pipe pressure drop per unit length	$\mathrm{kPa\,m}^{-1}$
$\dot{Q}$	heat transfer rate	W
R	ideal gas constant	$\mathrm{J\,mol}^{-1}\,\mathrm{K}^{-1}$
Re	Reynolds number	
R_f	fouling resistance	$\mathrm{m}^2\,\mathrm{K\,W}^{-1}$
T	temperature	K
U	overall heat transfer coefficient	$\mathrm{W\,m}^{-2}\,\mathrm{K}^{-1}$
v_{HU}	volume hold-up	m^3
V	voltage	V
$\dot{v}$	volume flow	$\mathrm{m}^3\,\mathrm{s}^{-1}$
$\dot{W}$	power	kW
β	plate chevron angle	° (degrees)
δ_{plate}	plate thickness	m
ϵ	pipe roughness factor	mm
ε	heat transfer effectiveness	
η_{pump}	pump efficiency	
μ	dynamic viscosity	Pa s
ρ	density	$\mathrm{kg\,m}^{-3}$

Subscripts

Subscript	Definition
c	cold fluid
ch	channel
cool	cooling load
crit	critical
eq	equivalent
h	hot fluid
i	inlet
LMTD	logarithmic mean temperature difference
loss	heat loss
m	mean
max	maximum
min	minimum
o	outlet
other	other equipment
PHE	plate heat exchanger
po	port
plate	plate
pump	pump
tn	thermoneutral voltage
v	vertical
w	width

1 Introduction

As more efforts prompt governments to boost decarbonization strategies and limit global warming to 1.5 °C agreed upon in 2015 by the United Nations with the Paris Agreement, the deployment of renewable energy (RE) systems is becoming a significant part of new policies for an energy transition from fossil fuels. A direct benefit of introducing RE systems is the reduction of CO_2 emissions, a well-known greenhouse gas (GHG) contributing to global warming. In Germany, the energy sector is responsible for more than 80 % of the total GHG emissions, and the electricity supply accounts for 40 % of the energy sector's emissions [1]. Given efficient energy production, storage, and distribution based on RE, 80-90 % of GHG emissions can be reduced by 2050 [2]. Consequently, the share of RE in the German electricity grid is increasing, reducing GHG emissions and bringing new challenges considering its intermittent production characteristics, triggering the curtailment of RE plants whenever transporting the generated power to end consumers can endanger the existing transmission infrastructure. The curtailment of RE plants decreases environmental benefits and increases costs, making it a concern in electric power systems [3].

To avoid curtailment of RE power plants, hydrogen produced with green electricity, known as green hydrogen, serves as chemical storage and an alternative to batteries, with significant potential to support energy transition. For green hydrogen production, proton exchange membrane (PEM) water electrolysis is suitable for fluctuating power input due to its response time compared with other water electrolysis technologies [4]. This is useful to provide grid stabilization services, e.g., avoid grid congestion, when directly coupled to the grid [5]. Since electrolysis assets are intended to be operated for several thousand hours, their reliable and long-term operation is essential in the energy transition roadmap.

The core of a proton exchange membrane water electrolysis (PEMWE) system consists of a set of electrochemical cells connected in series, known as a stack, where feed water is split into hydrogen and oxygen. During regular operation, the stack releases waste heat due to overcoming activation and ohmic overpotentials [6], increasing its temperature. The stack's temperature is a critical factor in its long-term reliable operation because high temperatures significantly accelerate the degradation rate of the membranes in the individual cells, leading to a permanent reduction in the stack's performance [7]. This highlights the importance of maintaining control over the feed water temperature in PEM electrolyzers.

1.1 Motivation

PEM electrolyzers are a key technology for the energy transition, so it is essential to guarantee their availability throughout their life cycle by controlling the feed water temperature. This requires comprehension of the dynamics of the stack as a source of waste heat and details of the cooling system in PEMWE systems supporting the stack's operation. Modeling enables the analysis of operating conditions with reduced time and effort compared to experimental approaches to understand the thermal behavior of PEMWE systems.

Olivier et al. [8] present an exhaustive overview of modeling works where the electrical, thermal, and fluidic domains of PEM electrolysis systems are covered, introducing the thermal model based on lumped parameters, which has been widely used as in the works of Espinosa-López et al. [9] and Rizwan et al. [10]. The lumped parameters thermal approach allows the modeling of a control volume representing the energy content of water involved in the electrolysis and its interactions with the surroundings, accounting for excess heat removal as a cooling load in the PEMWE cooling system. To the best of the author's knowledge, a detailed analysis of this cooling load in a plate heat exchanger (PHE) in PEM electrolysis has not been addressed in the literature presenting an opportunity for further exploration and understanding in the field.

The models for PHEs are based on first principles and empirical correlations, leading to non-linear models with cumbersome calculation routines due to the iterative calculation of thermodynamic fluid properties, for example. Additionally, the non-linear structure of PHE models is incompatible with integration with available multilinear time-invariant (MTI) models for multistack PEM electrolyzers. The MTI model class constitutes a powerful modeling tool as it approximates the non-linear behavior of basic non-linear phenomena, decreasing complexity and boosting simulation performance [11].

Due to the identified research gap in published literature and the advantages of MTI models, this thesis deals with the operation of the cooling system in PEM electrolyzers using a PHE to control feed water temperature, while investigating the MTI modeling approach to reduce the complexity of the cooling system model.

1.2 Aim of the thesis

This thesis aims to design an effective control strategy for the feed water temperature regulation in a PEM electrolyzer. To this end, a base model for a 1 MW PEM electrolyzer will be enhanced by incorporating a tailored-designed PHE and a PID controller in the electrolyzer's cooling system to analyze its thermal dynamics at different operating conditions. An MTI modeling approach is introduced to investigate its suitability

for modeling the PHE in this application. This PHE model will be coupled with a PID controller, which will dictate the required cooling water flow rate running through the PHE to achieve precise and effective feed water temperature control.
Additionally, a comprehensive hydraulic analysis based on the developed electrolyzer's model will be presented, contributing to establishing the power consumption of balance of plant (BOP) components associated with the electrolyzer's feed water and cooling system. This assessment aids in gaining a comprehensive understanding of energy consumption patterns in the electrolyzers, a crucial step toward optimizing power usage in BOP components.

1.3 Structure of the thesis

By the end of chapter 1, the reader should have a clear idea of the aim and structure of this thesis. Chapter 2 provides fundamental information for understanding the tools used for the analysis of cooling systems using PHE and their relevance in the context of PEM electrolyzers. Chapter 3 outlines the premises and characteristics of the selected equipment and systems to ensure the reproducibility of the results. In Chapter 4, a detailed description of the simulation results is provided, along with an analysis and discussion of the findings to offer insights into the performance and efficiency of the implemented models. Finally, Chapter 5 presents conclusions to the thesis by summarizing the key findings and giving an outlook on future research directions.

2 Fundamentals

This chapter delves into the essential knowledge required to comprehend the significance, modeling, and development of a temperature control strategy for the electrolyzer's feed water using a PHE. These key concepts are divided into seven parts for clarity and coherence.

The first part introduces PEMWE systems, focusing on the stack and its supporting BOP components in the cooling system, emphasizing their crucial role in the long-term functionality of the electrolyzer. The second part provides insights into heat transfer theory and energy balances, while the third part outlines the relationship of these concepts with the modeling and sizing of PHEs. The fourth part deals with the calculation of fluid thermodynamic properties needed to characterize the heat transfer process fully. The fifth part presents the system's description within the framework of state space models and modeling approaches explored in this thesis. The sixth part elaborates on the principles of control theory essential for designing a PID controller for the feed water temperature control. Lastly, a summary for analyzing power consumption in the BOP components associated with the electrolyzer's cooling system pumping equipment is presented.

2.1 Proton exchange membrane water electrolyzers

The core of a PEMWE system is the electrolysis cells, where the water electrolysis reaction takes place, splitting water into hydrogen and oxygen. Figure 2.1 presents the structure of a PEM cell, which consists of electrode layers (anode and cathode), an ionic conductor (membrane), and electronic conductors (distribution plates), all of which facilitate the electrolysis reaction

$$2\,\mathrm{H_2O} \longrightarrow 2\,\mathrm{H_2} + \mathrm{O_2}. \tag{2.1}$$

For this reaction to take place a minimum voltage V_{tn}, known as thermoneutral or reversible voltage, has to be applied to the cell. At standard conditions V_{tn} corresponds to 1.23 V. However, the actual cell voltage V_{cell} is higher than V_{tn} due to irreversibilities attributed to activation, ohmic, and concentration overpotentials in the cell [12]. The relationship between these overpotentials and the thermoneutral voltage at different current densities can be represented in polarization curves as shown in Figure 2.2.

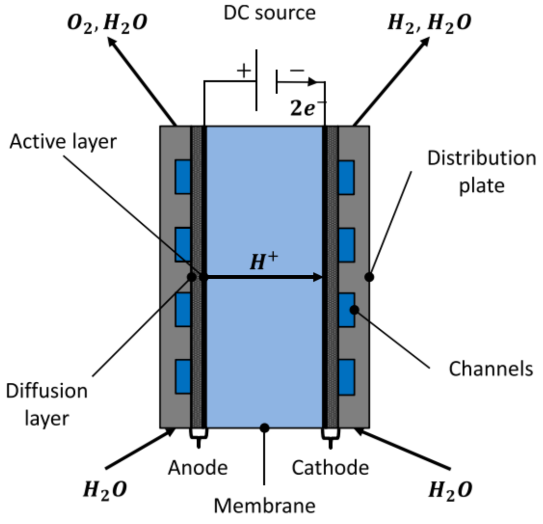

Anode	$H_2O \rightarrow \frac{1}{2}O_2 + 2H^+ + 2e^-$
Cathode	$2H^+ + 2e^- \rightarrow H_2$
Total reaction	$H_2O \rightarrow \frac{1}{2}O_2 + H_2$

Figure 2.1: Schematic of the operation principle of a PEMWE cell [8].

For large-scale operation, cells are connected in series using distribution plates, creating stacks whose geometry provides flow channels for reagent feed and product evacuation. In these stack assemblies, the electrical energy loss released as heat due to overpotentials corresponds to

$$\dot{W}_{\text{stack,heat}} = (V_{\text{cell}} - V_{\text{tn}})\, i\, n_{\text{cell}}, \tag{2.2}$$

with the electric current density i, and the number of cells in the stack n_{cell} [9]. In addition to the voltage requirement, the PEM cell requires a minimum amount of feed water for the electrolysis reaction, which is given by

$$\dot{n}_{\text{H}_2\text{O,min}} = \frac{n_{\text{cell}} I}{2F}, \tag{2.3}$$

with the current I, and the faraday constant F. Stacks are connected to auxiliary systems, known as balance of plant (BOP) components, to support stack operation; for example, by removing $\dot{W}_{\text{stack,heat}}$ absorbed by the feed water as high temperature triggers degradation mechanisms in the cell membranes, reducing the stack's lifetime and performance. To this end, in practice, the feed water stream is set in a condition such that $\dot{n}_{\text{H}_2\text{O}} >> \dot{n}_{\text{H}_2\text{O,min}}$, and coupled with a cooling water stream for thermal interaction in a heat exchanger (HE). This fundamental configuration constitutes the cooling system of the electrolyzer, which is further elaborated later in this section. Additional BOP com-

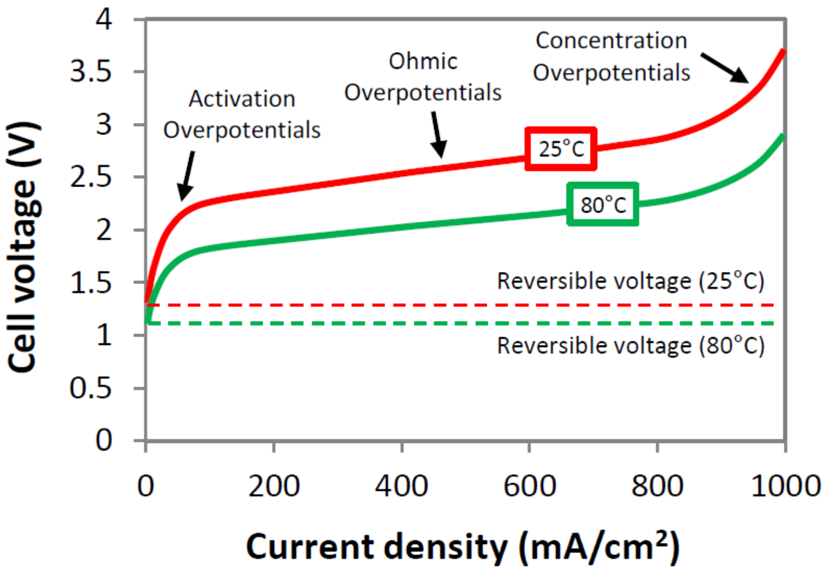

Figure 2.2: Polarization curve of an electrolysis cell [12].

ponents of the electrolyzer are responsible for adapting the input power to the stack and controlling salt concentration in the feed water, as these can negatively affect the stack performance [4, 8]. Figure 2.3 presents an overall block diagram of a typical PEMWE system, including complementary BOP components related to hydrogen conditioning for storage or transportation. Figure 2.3 highlights the cooling system as it is the focus of study in this thesis.

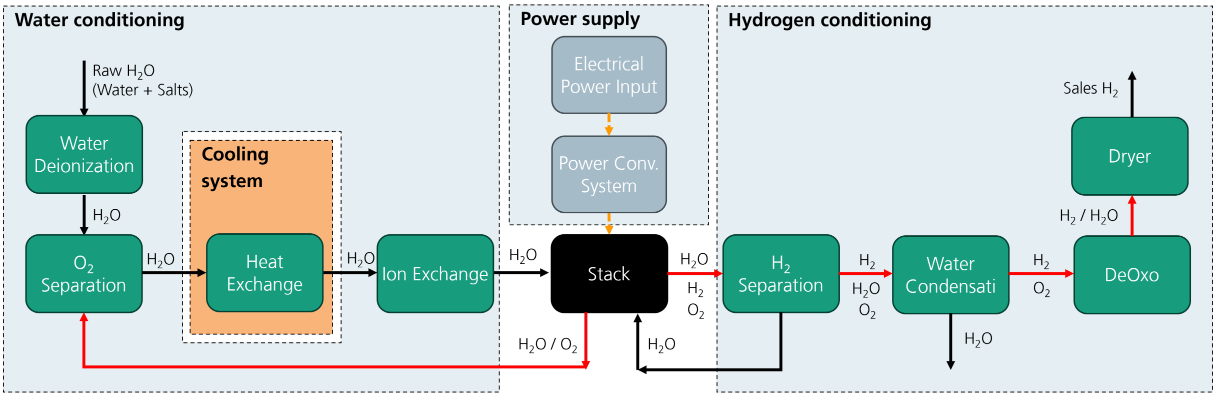
Water conditioning
Raw H₂O (Water + Salts)
Water Deionization
H₂O
O₂ Separation
H₂O
Cooling system
Heat Exchange
H₂O
Ion Exchange
Power supply
Electrical Power Input
Power Conv. System
H₂O
Stack
H₂O / O₂
H₂O
H₂O
H₂
O₂
Hydrogen conditioning
H₂ Separation
H₂
H₂O
O₂
Water Condensati
H₂O
H₂
O₂
DeOxo
H₂ / H₂O
Dryer
Sales H₂

Figure 2.3: Block diagram of a PEMWE system
(Own figure based on [8]).

The cooling system consists of a HE that couples the feed water circuit with a cooling water circuit to cool down the feed water stream entering the electrolysis stack as shown in Figure 2.4. Here, the temperature control of the feed water stream is achieved by measuring its temperature at the stack's outlet and processing this signal in a temperature controller to produce an output signal dictating the required flow in the cooling water circuit. For reliable long-term electrolyzer operation, the controller must maintain the desired temperature level whenever substantial variations of the power input to the electrolysis stack occur. Figure 2.4 also shows the required electrical connection of the pumps, as energy is invested in keeping water circulating in both circuits. Hereafter, hot fluid and cold fluid are used interchangeably to refer to the feed water and cooling water, respectively.

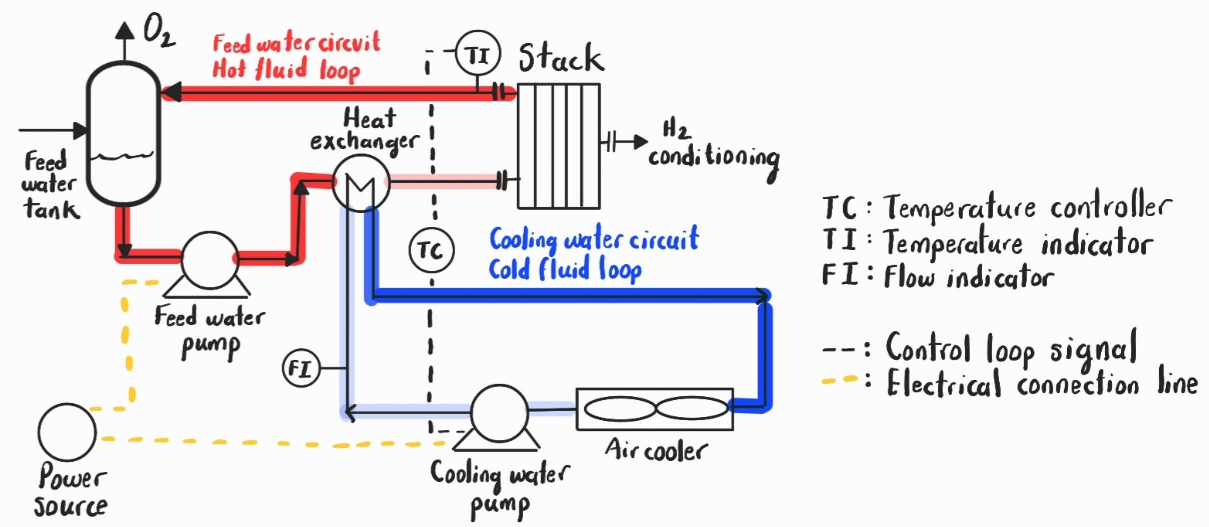
O_2
Feed water circuit
Hot fluid loop
TI
Stack
Heat exchanger
H_2 conditioning
Feed water tank
TC
Cooling water circuit
Cold fluid loop
Feed water pump
FI
Air cooler
Power source
Cooling water pump
TC : Temperature controller
TI : Temperature indicator
FI : Flow indicator
-- : Control loop signal
-- : Electrical connection line

Figure 2.4: Feed water cooling system of a PEM electrolyzer
(Own figure based on [13–16]).

2.2 Heat transfer theory

The information presented in this chapter section is mainly taken from Rizwan et al. [10], L. Wang, B. Sundén, R.M. Manglik [17], and Kakaç et al. [18]. Other sources are marked accordingly.

2.2.1 Energy balances

In a heat transfer operation, hot and cold fluid streams interact, separated by a thermal conductive plate, allowing heat flow from the hot stream to the cold stream while avoiding the mixing of both fluids. This arrangement constitutes the fundamental notion of a HE, where the fluids can flow in co-current (parallel in the same direction) or counter-current (parallel in opposite directions), generating different heat transfer dynamics. Because counter-current flow is more efficient than co-current flow arrangement, it requires less heat transfer area [19] and will therefore be further analyzed. Figure 2.5 illustrates the heat transfer between two fluids in a counter-current flow arrangement with the heat flow $\dot{Q}$, the mass flow $\dot{m}$ and the temperature T. Subscripts h and c identify hot and cold fluid, while i and o identify HE inlet and outlet.

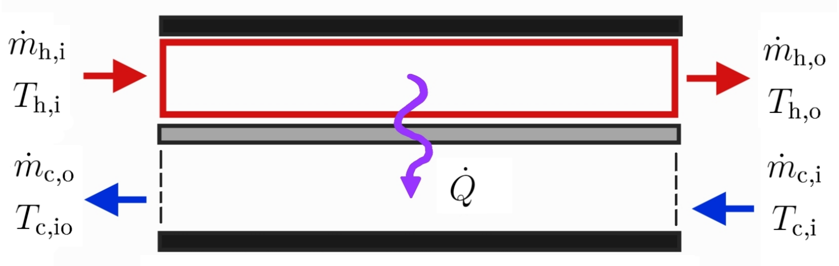

Figure 2.5: Heat transfer across a conductive plate.

The energy content of the hot fluid can be analysed by writing down the corresponding mass and energy balances for the control volume shown as a red rectangle in Figure 2.5. For an open system with steady state flow conditions the mass balance reads

$$\dot{m}_{\mathrm{h,i}} = \dot{m}_{\mathrm{h,o}} = \dot{m}_{\mathrm{h}}. \tag{2.4}$$

The first law of thermodynamics applied to the same system with negligible changes in the potential and kinetic energy leads to the energy balance

$$\left(\rho_{\mathrm{h}} v_{\mathrm{HU_h}} c_{p_{\mathrm{h}}}\right) \frac{\mathrm{d}T_{\mathrm{h,o}}}{\mathrm{d}t} = \dot{m}_{\mathrm{h}} c_{p_{\mathrm{h}}} \left(T_{\mathrm{h,i}} - T_{\mathrm{h,o}}\right) - \dot{Q}, \tag{2.5}$$

with the fluid density ρ, the volume hold-up v_{HU}, and the heat capacity c_p. This equation describes the change in the control volume's energy content in terms of the energy inflow and outflow carried by the hot stream minus the energy flowing across the conductive plate to the cold fluid.

An analogous analysis for the cold fluid delivers

$$\left(\rho_{\mathrm{c}} v_{\mathrm{HU_c}} c_{p_{\mathrm{c}}}\right) \frac{\mathrm{d}T_{\mathrm{c,o}}}{\mathrm{d}t} = \dot{m}_{\mathrm{c}} c_{p_{\mathrm{c}}} \left(T_{\mathrm{c,i}} - T_{\mathrm{c,o}}\right) + \dot{Q}. \tag{2.6}$$

2.2.2 Heat transfer relationships

As shown in (2.5) and (2.6), to solve the energy balances the heat flow $\dot{Q}$ is required, which calculation corresponds to

$$\dot{Q} = UA\Delta T_{\mathrm{m}}, \tag{2.7}$$

with the HE's total transfer area A, the overall heat transfer coefficient U, and the mean temperature difference ΔT_{m}. This mean temperature difference ΔT_{m} conveniently represents the variation of the temperature difference between hot and cold fluids with the position along the HE and should be understood as the thermal driving force of the transfer process. The overall heat transfer coefficient U depends on the convective and fouling resistances in the two fluid streams, and the thermal resistance due to conduction through the plate thicknesss. Figure 2.6 presents a scheme of the temperature variation between hot and cold fluid and its corresponding thermal resistances.

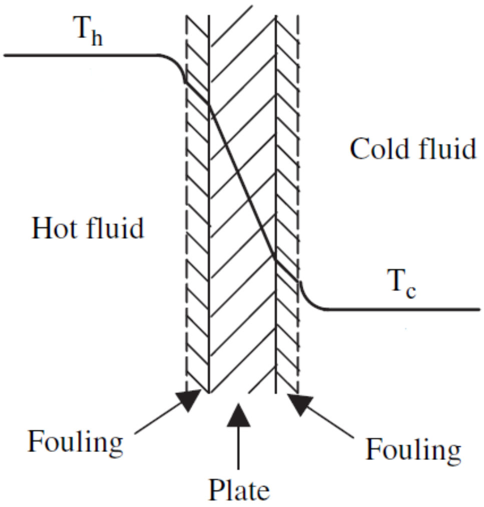

Figure 2.6: Thermal resistances across a conductive plate [10].

The overall heat transfer coefficient can be calculated as

$$\frac{1}{U} = \frac{1}{h_\mathrm{h}} + \frac{1}{h_\mathrm{c}} + \frac{\delta_\mathrm{plate}}{k_\mathrm{plate}} + R_{f_\mathrm{h}} + R_{f_\mathrm{c}}, \tag{2.8}$$

with the heat transfer coefficient h, the plate thickness δ_plate, the thermal conductivity of the plate material k_plate, and the fouling resistance R_f.

2.2.3 Thermal methods for heat exchangers

This section covers the logarithmic mean temperature difference (LMTD) and the ε-NTU method due to its wide use in industry. Other methods, such as the P-NTU are not relevant here but discussed in [20].

Logarithmic mean temperature difference (LMTD)

A differential energy balance accounting for the heat transfer across an arbitrary area element, dA, can be expressed as

$$\mathrm{d}\dot{Q} = U\,\mathrm{d}A\,\Delta T = U\,\mathrm{d}A\,(T_\mathrm{h} - T_\mathrm{c})\,. \tag{2.9}$$

Alternatively, this energy balance can be expressed as

$$\mathrm{d}\dot{Q} = -C_\mathrm{h}\mathrm{d}T_\mathrm{h} = \pm C_\mathrm{c}\mathrm{d}T_\mathrm{c}, \tag{2.10}$$

with the heat capacity rates for the hot and cold fluid C_h and C_c, respectively, given by

$$\begin{aligned} C_\mathrm{h} &= \dot{m}_\mathrm{h} c_{p_\mathrm{h}}, \\ C_\mathrm{c} &= \dot{m}_\mathrm{c} c_{p_\mathrm{c}}. \end{aligned} \tag{2.11}$$

Expressing the temperature difference between the fluids in a counter-current arrangement leads to

$$\mathrm{d}(T_\mathrm{h} - T_\mathrm{c}) = \mathrm{d}T_\mathrm{h} - \mathrm{d}T_\mathrm{c} = \mathrm{d}\dot{Q}\left(\frac{1}{C_\mathrm{c}} - \frac{1}{C_\mathrm{h}}\right), \tag{2.12}$$

whose combination with (2.9) delivers

$$\dot{Q} = UA\frac{(T_\mathrm{h,i} - T_\mathrm{c,o}) - (T_\mathrm{h,o} - T_\mathrm{c,i})}{\ln\left(\frac{T_\mathrm{h,i}-T_\mathrm{c,o}}{T_\mathrm{h,o}-T_\mathrm{c,i}}\right)}. \tag{2.13}$$

By comparing (2.13) with (2.7), it follows that an appropriate mean temperature difference across a counter-current HE can be expressed as

$$\Delta T_\mathrm{m} = \frac{(T_\mathrm{h,i} - T_\mathrm{c,o}) - (T_\mathrm{h,o} - T_\mathrm{c,i})}{\ln\left(\frac{T_\mathrm{h,i}-T_\mathrm{c,o}}{T_\mathrm{h,o}-T_\mathrm{c,i}}\right)} = \Delta T_\mathrm{LMTD}. \tag{2.14}$$

This corresponds to the mathematical definition of the LMTD for quantifying the thermal driving force in counter-current HEs [18]. Considering the natural logarithm $\ln(x)$ in (2.14) is defined for the domain $\{x \in \mathbb{R} | x > 0\}$, whenever $T_\mathrm{h,i} < T_\mathrm{c,o}$ or $T_\mathrm{h,o} < T_\mathrm{c,i}$, $\Delta T_\mathrm{LMTD} = 0$.

The ε-NTU method

The LMTD method is suited for cases where both fluids' inlet and outlet temperatures are known. When these temperatures are not available, the thermal analysis can be carried out using the ε-NTU method relying on the following dimensionless parameters [18]:

1. **Heat capacity rate ratio**
   By definition the heat capacity rate C^* is given by

   $$C^* = \frac{C_\mathrm{min}}{C_\mathrm{max}}, \tag{2.15}$$

   with C_min and C_max corresponding to the smaller and larger heat capacity rates of the hot and cold fluid. Here, $C^* \leq 1$.

2. **Effectiveness**
   The effectiveness ε is the ratio of the actual heat flow to the thermodynamically

limited maximum possible heat flow

$$\varepsilon = \frac{\dot{Q}}{\dot{Q}_{\max}}. \tag{2.16}$$

The actual heat flow $\dot{Q}$ can be estimated from an energy balance either on the hot or cold fluid according to

$$\dot{Q} = \left(\dot{m}c_p\right)_{\mathrm{h}} \left(T_{\mathrm{h,i}} - T_{\mathrm{h,o}}\right) = \left(\dot{m}c_p\right)_{\mathrm{c}} \left(T_{\mathrm{c,o}} - T_{\mathrm{c,i}}\right). \tag{2.17}$$

The calculation of the maximum possible heat flow $\dot{Q}_{\max}$ considers the fluid undergoing the maximum temperature difference as the fluid with the minimum heat capacity rate

$$\dot{Q}_{\max} = \begin{cases} \left(\dot{m}c_p\right)_{\mathrm{c}} \left(T_{\mathrm{h,i}} - T_{\mathrm{c,i}}\right) & \text{if } C_{\mathrm{c}} < C_{\mathrm{h}}, \\ \left(\dot{m}c_p\right)_{\mathrm{h}} \left(T_{\mathrm{h,i}} - T_{\mathrm{c,i}}\right) & \text{if } C_{\mathrm{h}} < C_{\mathrm{c}}. \end{cases} \tag{2.18}$$

Combination of (2.16) to (2.18) delivers

$$\varepsilon = \frac{C_{\mathrm{h}} \left(T_{\mathrm{h,i}} - T_{\mathrm{h,o}}\right)}{C_{\min} \left(T_{\mathrm{h,i}} - T_{\mathrm{c,i}}\right)} = \frac{C_{\mathrm{c}} \left(T_{\mathrm{c,o}} - T_{\mathrm{c,i}}\right)}{C_{\min} \left(T_{\mathrm{h,i}} - T_{\mathrm{c,i}}\right)}. \tag{2.19}$$

Additionally, the actual heat transfer $\dot{Q}$ can be expressed as

$$\dot{Q} = \varepsilon \left(\dot{m}c_p\right)_{\min} \left(T_{\mathrm{h,i}} - T_{\mathrm{c,i}}\right). \tag{2.20}$$

3. **Number of transfer units**

   The number of transfer units (NTU) designates the dimensionless size of a HE

$$\mathrm{NTU} = \frac{AU}{C_{\min}} = \frac{1}{C_{\min}} \int_A U \,\mathrm{d}A. \tag{2.21}$$

Figure 2.7 presents the graphical relationship between C^*, ε, and NTU given by

$$\varepsilon = \frac{1 - \exp\left[-(1 - C^*)\mathrm{NTU}\right]}{1 - C^* \exp\left[-(1 - C^*)\mathrm{NTU}\right]}, \tag{2.22}$$

$$\mathrm{NTU} = \frac{1}{1 - C^*} \ln\left(\frac{1 - \varepsilon\, C^*}{1 - \varepsilon}\right). \tag{2.23}$$

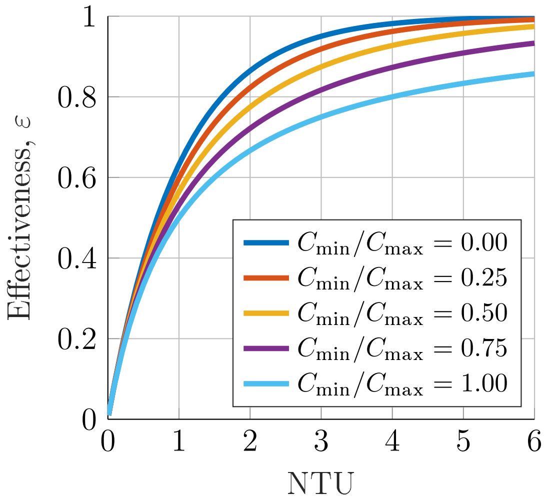

Figure 2.7: Relationship ε-NTU for counter-current flow arrangement.

2.3 PHEs

For PEMWE, the electrolysis systems can be delivered as containerized units ready to be plugged in and operated. Multiple vendors, such as Nel Hydrogen [13, 14], Teledyne Energy Systems [15], Plug Power Inc. [16], and H-TEC Systems [21], have incorporated PHEs as standard equipment in the electrolyzers cooling system. Therefore, PHEs characteristics are further studied.

2.3.1 Configuration and assembly

Depending on the leak tightness required during service, PHEs can be classified into gasketed, welded, and brazed, with the gasketed type being the most common one [22]. Figure 2.8 presents the basic construction of a gasketed PHE, which consists of thin rectangular metal plates held together by a frame. Long bolts clamp the plates together and form a seal, which is achieved by compressing gaskets placed between them. Each plate has a corrugated surface design intended to provide rigidity to the plate structure and induce fluid turbulence, thereby defining the thermal and hydraulic behavior of the PHE. It is worth noting that most corrugation designs of the plates are proprietary and not published [23]. Standard corrugated plate patterns and geometries are presented in Figure 2.9, with the chevron pattern being prevalent among general applications [22]. Regarding the flow arrangement, counter-current is typically used with a single or multiple passes per fluid. A U-pass arrangement is preferred whenever a single-pass counter-current PHE is used, as it connects fluid inlets and outlets on the same side of the HE (Figure 2.10).

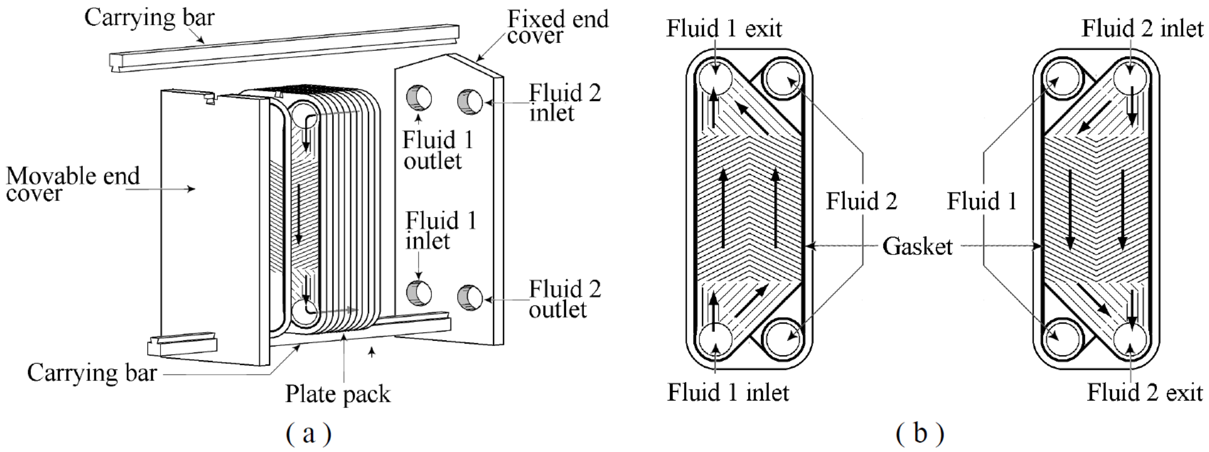
Carrying bar
Fixed end cover
Fluid 2 inlet
Fluid 1 outlet
Movable end cover
Fluid 1 inlet
Fluid 2 outlet
Carrying bar
Plate pack
(a)
Fluid 1 exit
Fluid 2 inlet
Fluid 2
Fluid 1
Gasket
Fluid 1 inlet
Fluid 2 exit
(b)

Figure 2.8: Gasketed PHE: (a) assembly; (b) individual plates [22].

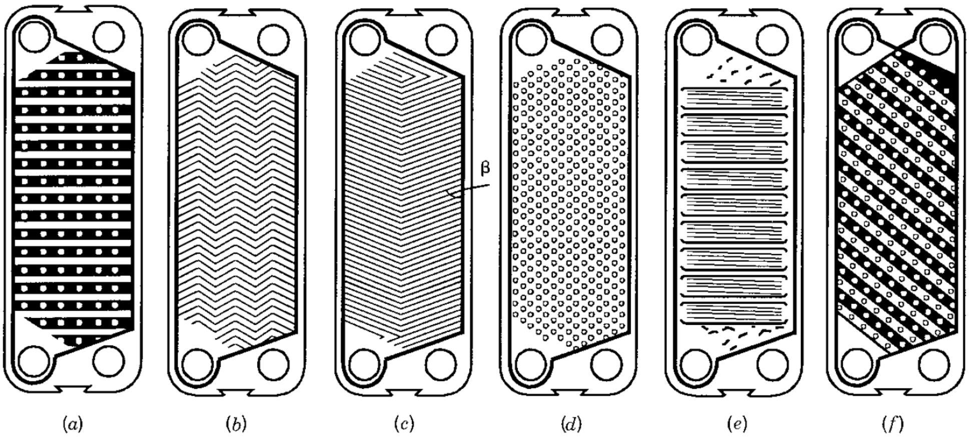

Figure 2.9: Plate patterns: (a) washboard; (b) zigzag; (c) chevron or herringbone; (d) protrusions and depressions; (e) washboard with secondary corrugations; (f) oblique washboard [24].

2.3.2 Thermal and hydraulic correlations

In subsection 2.3.1 it is noted that the designs of the corrugations on the plates are typically proprietary and not publicly available, resulting in a lack of heat transfer correlations in the literature [24]. Despite limited information being accessible in published works, Kakaç et al. [18] provide an extensive overview of available correlations for chevron plates, from which relevant excerpts are included in this section. A detailed schematic of a chevron plate, defined by the corrugation angle or chevron angle β, is illustrated in Figure 2.11, where the plate's effective heat transfer area is determined by

$$A_{\text{plate,e}} = \phi \, A_{\text{plate,p}}, \tag{2.24}$$

with the plate enlargement factor ϕ, and the plate projected area $A_{\text{plate,p}}$. The plate enlargement factor ϕ varies from 1.15 to 1.25 being a function of the corrugation pitch

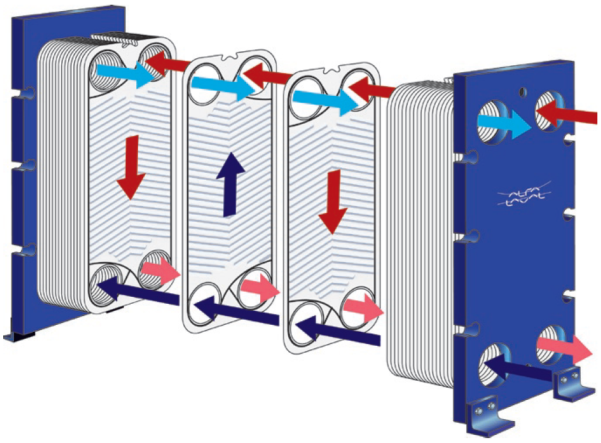

Figure 2.10: Gasketed PHE: single pass, counterflow and U-pass flow arrangement [25].

and depth. The plate projected area is calculated using

$$A_{\text{plate,p}} = L_{\text{p}}\, L_{\text{w}}, \tag{2.25}$$

with the plate projected length L_{p} and the plate width inside gaskets L_{w}. For the thermal and hydraulic analysis of PHEs using chevron plates, the correlation proposed by H. Kumar [26] is particularly valuable as it takes into account the impact of fluid stream conditions and plate geometry by incorporating the Reynolds number in plate channels

$$Re_{\text{ch}} = \left(\frac{d_{\text{ch}} G_{\text{ch}}}{\mu}\right), \tag{2.26}$$

with the channel hydraulic diameter d_{ch}, the mass velocity through a channel G_{ch}, and the fluid viscosity μ. The fluid's mass velocity through a channel G_{ch} is given by

$$G_{\text{ch}} = \left(\frac{\dot{m}}{n_{\text{ch,p}} b L_{\text{w}}}\right), \tag{2.27}$$

with the number of channels per pass $n_{\text{ch,p}}$ and the mean plate channel gap b. The heat transfer coefficient h, required for the estimation of the overall heat transfer coefficient U in (2.8), equals

$$\frac{h\, d_{\text{ch}}}{k} = C_{\text{ch}} \left(\frac{d_{\text{ch}} G_{\text{ch}}}{\mu}\right)^{n} \left(\frac{c_p \mu}{k}\right)^{1/3} \left(\frac{\mu}{\mu_{\text{w}}}\right)^{0.17}, \tag{2.28}$$

with the channel constant C_{ch}, the fluid thermal conductivity k, and the fluid viscosity at wall temperature μ_{w}. Here the thermal parameters C_{ch} and n are function of Re_{ch} and β. Regarding the hydraulic analysis, the channel friction factor f_{ch} is calculated by

$$f_{\text{ch}} = \frac{K_{\text{ch}}}{(Re_{\text{ch}})^{m}}, \tag{2.29}$$

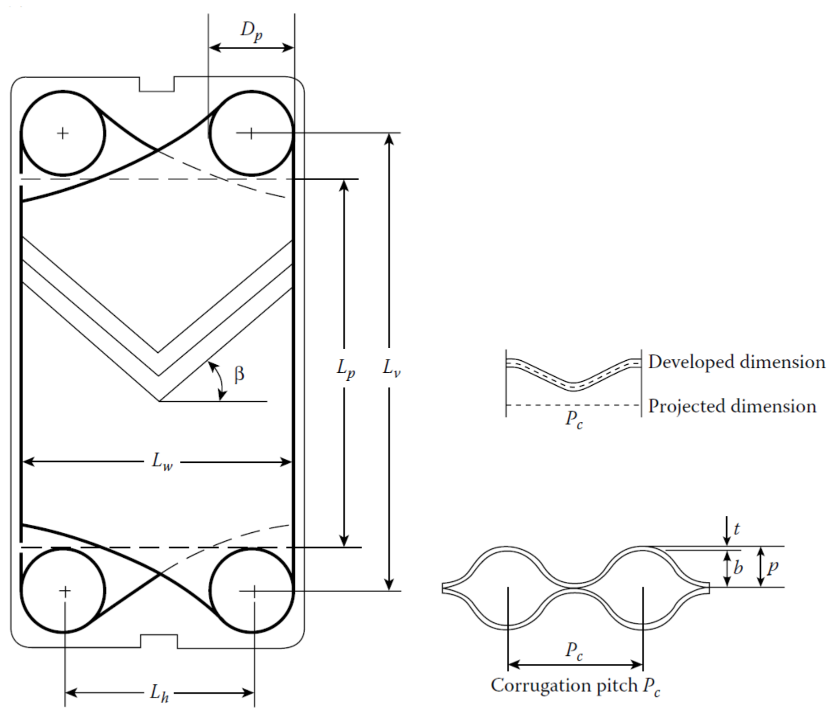
D_p
β
L_p
L_v
L_w
L_h
Developed dimension
Projected dimension
P_c
t
b
p
P_c
Corrugation pitch P_c

Figure 2.11: Main dimensions of a chevron plate [18].

with the hydraulic parameters K_{ch} and m depending on Re_{ch} and β. Table 2.1 summarizes the relationship between the correlations' parameters, the fluid flow characteristics and plate geometry.

2.3.3 Sizing

To achieve a viable design for sizing a PHE, the thermal energy levels of the streams involved must be analyzed. Figure 2.12 presents a schematic representation of a counter-flow single-pass PHE, with sides A and B indicating where the hot stream enters and exits the PHE.

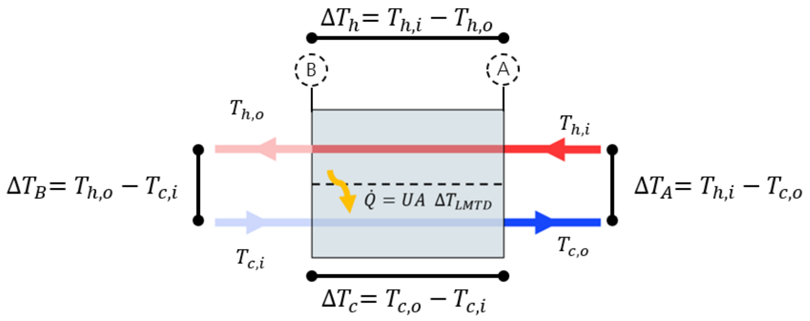
$\Delta T_h = T_{h,i} - T_{h,o}$
B
A
$T_{h,o}$
$T_{h,i}$
$\Delta T_B = T_{h,o} - T_{c,i}$
$\dot{Q} = UA\ \Delta T_{LMTD}$
$\Delta T_A = T_{h,i} - T_{c,o}$
$T_{c,i}$
$T_{c,o}$
$\Delta T_c = T_{c,o} - T_{c,i}$

Figure 2.12: Counter-flow PHE schematic
(Own figure based on [18]).

Table 2.1: Constants for single-phase heat transfer correlation in gasketed PHE [18].

β (degree)	Heat transfer			Pressure loss		
	Re_{ch}	C_{ch}	n	Re_{ch}	K_{ch}	m
<30	<10	0.718	0.349	<10	50	1
	>10	0.348	0.663	10-100	19.4	0.589
				>100	2.99	0.183
45	<10	0.718	0.349	<15	47	1
	10-100	0.4	0.598	15-300	18.29	0.652
	>100	0.3	0.663	>300	1.441	0.206
50	<20	0.63	0.333	<20	34	1
	20-300	0.291	0.591	20-300	11.25	0.631
	>300	0.13	0.732	>300	0.772	0.161
60	<20	0.562	0.326	<40	24	1
	20-400	0.306	0.529	40-400	3.24	0.457
	>400	0.108	0.703	>400	0.76	0.215
≥ 65	<20	0.562	0.326	50	24	1
	20-500	0.331	0.503	50-500	2.8	0.451
	>500	0.087	0.718	>500	0.639	0.213

The temperature differences on the sides of the PHE ΔT_{A} and ΔT_{B}, known as temperature approaches, are crucial for predicting the thermal performance of the designed PHE. These temperature approaches have a direct impact on the size of the PHE. As these approaches decrease, the size of the PHE increases. Therefore, it is of utmost importance to establish and adhere to practical guidelines to ensure the design of appropriately sized equipment. For PHEs, close temperature approaches are allowed [27]. Even a one-degree Celsius temperature approach can occur due to the high degree of counter-current flow [28]. Additionally, counter-current flow allows operation with crossing temperatures, meaning the cold fluid can have a higher exiting temperature than the exiting hot fluid [29]. Regarding the individual temperature change of the fluids, ΔT_{h}, is determined based on the cooling requirements, while the change in cold temperature, ΔT_{c}, is influenced by the properties of the cooling water and the treatment of return water (the cooling water from the PHE). For the electrolysis system under analysis in this thesis, an air cooler is used to lower the temperature of the return water before flowing back to the PHE (Figure 2.4). According to Walas [30] the recommended temperature range for the cooling water supply with air cooling is $26\ {}^\circ\mathrm{C} < T_{\mathrm{c,i}} < 32\ {}^\circ\mathrm{C}$ to ensure optimal thermal performance, accounting for seasons with high ambient temperatures. The return water temperature, $T_{\mathrm{c,o}}$, is established by practical temperature approaches of 27 °C [30] in air coolers, resulting in $53\ {}^\circ\mathrm{C} < T_{\mathrm{c,o}} < 59\ {}^\circ\mathrm{C}$.

These guidelines and insights can be applied in the ε-NTU sizing method to calculate the total heat transfer area. PHEs can achieve high thermal performance, with ε values exceeding 0.9 attainable with very small temperature approaches [18, 28]. Most PHEs have NTU values ranging from 0.5 to 4.0, with 2.0 and 3.0 being the most common [27]. Figure 2.13 provides a graphical representation of the area where the designed PHE for the PEMWE system is to be located, taking into account the aforementioned temperature approach guidelines.

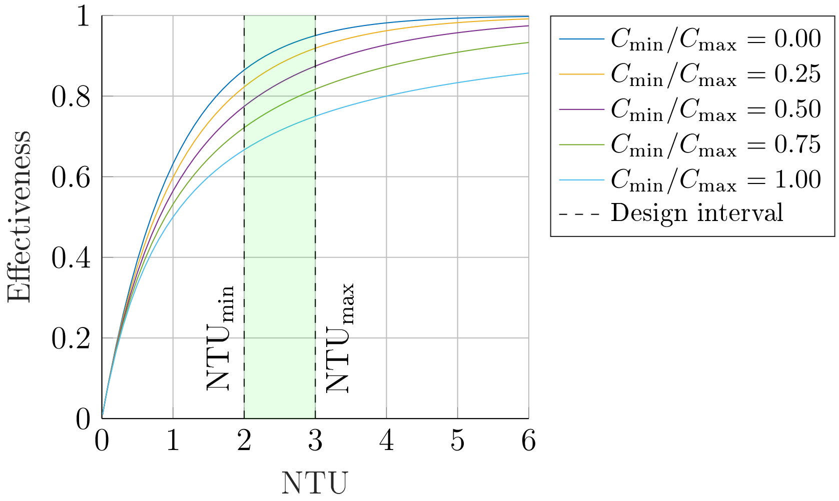

Figure 2.13: NTU interval for PHE design.

2.4 Estimation of thermodynamic properties

The solution of energy balances in (2.5) and (2.6) requires knowledge about the thermodynamic properties of pure water and cooling water used. For single-phase liquid-cooling applications, aqueous ethylene or propylene glycol mixtures are the most widely used [31]. Therefore, the aqueous solution of propylene glycol 38 % (PG38 %) is selected as cooling water for further analysis.

Verein Deutscher Ingenieure et al. [32, Section D3.1] provides experimental data and correlations for property estimation of pure water in the saturated liquid state. Fundamental and critical properties of water needed for these correlations are presented in Table 2.2.

Table 2.2: Fundamental and critical properties of pure water [32].

Substance	Formula	M ($\mathrm{g\,mol^{-1}}$)	T_{crit} (K)	ρ_{crit} ($\mathrm{kg\,m^{-3}}$)
Water	H_2O	18.02	647.1	322

For PG38 %, table sets of properties at different temperatures are available in [32, Section D4.2]. To incorporate this data consistently into the model, the properties of PG38 % are fitted to the polynomial structure of the water correlations. The parameters are fitted assuming PG38 %'s fundamental and critical properties are equal to the properties of pure water in Table 2.2. In the following, the relevant correlations for property estimation of water and PG38 % are presented, highlighting their validity in the interval $273.15\text{ K} \leq T \leq 373.15\text{ K}$ suitable for PEMWE applications:

1. Liquid density:

$$\begin{aligned}\rho = \rho_{\text{crit}} + A\left(1 - \frac{T}{T_{\text{crit}}}\right)^{0.35} + B\left(1 - \frac{T}{T_{\text{crit}}}\right)^{2/3} \\ +C\left(1 - \frac{T}{T_{\text{crit}}}\right) + D\left(1 - \frac{T}{T_{\text{crit}}}\right)^{4/3}.\end{aligned} \tag{2.30}$$

Table 2.3: Parameters for liquid density estimation (Adapted from [32, Section D3.1 Table 2]).

Substance	Formula	A	B	C	D
Water	H_2O	1094	-1813	3864	-2480
PG38 %	-	21653	-76230	96130	-41163

2. Liquid dynamic viscosity:

$$\mu = E \cdot \exp\left[A\left(\frac{C-T}{T-D}\right)^{1/3} + B\left(\frac{C-T}{T-D}\right)^{4/3}\right]. \tag{2.31}$$

Table 2.4: Parameters for liquid dynamic viscosity estimation (Adapted from [32, Section D3.1 Table 7]).

Substance	Formula	A	B	C	D	E
Water	H_2O	0.45	1.40	613.18	63.70	6.90×10^{-5}
PG38 %	-	-35.38	-63.43	59.66	-40.10	13.24

3. Liquid thermal conductivity:

$$k = A + BT + CT^2 + DT^3 + ET^4. \tag{2.32}$$

Table 2.5: Parameters for liquid thermal conductivity estimation (Adapted from [32, Section D3.1 Table 9]).

Substance	Formula	A	B	C	D	E
Water	H_2O	-2.41	2.45×10^{-2}	-7.31×10^{-5}	9.95×10^{-8}	-5.37×10^{-11}
PG38 %	-	-0.41	9.86×10^{-3}	-4.49×10^{-5}	9.24×10^{-8}	-7.10×10^{-11}

4. Liquid specific heat capacity:

$$\begin{aligned}c_p = R\Bigg(\frac{A}{1-\frac{T}{T_{\text{crit}}}} + B + C\left(1 - \frac{T}{T_{\text{crit}}}\right) + D\left(1 - \frac{T}{T_{\text{crit}}}\right)^2 \\ +E\left(1 - \frac{T}{T_{\text{crit}}}\right)^3 + F\left(1 - \frac{T}{T_{\text{crit}}}\right)^4\Bigg),\end{aligned} \tag{2.33}$$

with the ideal gas constant R.

Table 2.6: Parameters for liquid specific heat capacity estimation

(Adapted from [32, Section D3.1 Table 5]).

Substance	Formula	A	B	C	D	E	F
Water	H_2O	0.2	12.9	-33.6	104.8	-155.5	92.4
PG38 %	-	-50.6	501.6	-1904.6	3666.1	-3530.2	1359.6

2.5 State space models

Models of real systems allow for a deeper understanding of the behavior of the systems, facilitating analysis, control, or the development of new concepts with reduced time and effort compared to experimental approaches. Consider the general system depicted in Figure 2.14, where the input $\mathbf{u}$ provided to the system generates the output $\mathbf{y}$. Here, $\mathbf{u} \in \mathbb{R}^m$ and $\mathbf{y} \in \mathbb{R}^p$, while the current state of the system is described by the states $\mathbf{x} \in \mathbb{R}^n$. Other domains different from the real domain are not relevant to this thesis but are discussed in Pangalos [33].

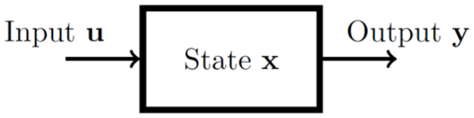

Figure 2.14: General system with inputs, outputs and states.

For the description of states, it has been acknowledged that state space models formulated on differential equations can provide a satisfactory representation of real systems. A general description of nonlinear continuous-time state space models corresponds to

$$\dot{\mathbf{x}}(t) = \mathbf{f}(\mathbf{x}(t), \mathbf{u}(t)) = (f_1(\mathbf{x}, \mathbf{u}) \dots f_n(\mathbf{x}, \mathbf{u}))^{\mathsf{T}}, \tag{2.34}$$

$$\dot{\mathbf{y}}(t) = \boldsymbol{g}(\mathbf{x}(t), \mathbf{u}(t)) = (g_1(\mathbf{x}, \mathbf{u}) \dots g_p(\mathbf{x}, \mathbf{u}))^{\mathsf{T}}, \tag{2.35}$$

$$\mathbf{x}(0) = \mathbf{x}_0, \tag{2.36}$$

with time t and initial state $\mathbf{x}_0$.

2.5.1 Linear time-invariant (LTI) models

The system of n first-order differential equations shown in (2.34) and (2.35) can be approximated by a general linear system

$$\dot{\mathbf{x}}(t) = \mathbf{A}(t)\mathbf{x}(t) + \mathbf{B}(t)\mathbf{u}(t), \tag{2.37}$$

$$\dot{\mathbf{y}}(t) = \mathbf{C}(t)\mathbf{x}(t) + \mathbf{D}(t)\mathbf{u}(t), \tag{2.38}$$

with the dynamics matrix $\mathbf{A}(t) \in \mathbb{R}^{n\times n}$, the input matrix $\mathbf{B}(t) \in \mathbb{R}^{n\times m}$, the output matrix $\mathbf{C}(t) \in \mathbb{R}^{p\times n}$, and the feedthrough matrix $\mathbf{D}(t) \in \mathbb{R}^{p\times m}$ [34]. When the matrixes $\mathbf{A}$, $\mathbf{B}$, $\mathbf{C}$, and $\mathbf{D}$ are time independent, the system is denominated LTI state system and simplified to

$$\dot{\mathbf{x}}(t) = \mathbf{A}\mathbf{x}(t) + \mathbf{B}\mathbf{u}(t), \tag{2.39}$$

$$\dot{\mathbf{y}}(t) = \mathbf{C}\mathbf{x}(t) + \mathbf{D}\mathbf{u}(t). \tag{2.40}$$

For the description of the thermal system in (2.5) and (2.6), the outlet temperatures of the HE correspond to the states and the outputs of the state space system, meaning $\mathbf{x}(t) = \mathbf{y}(t)$. Therefore an addtional output function as in (2.40) is not considered in this thesis.

2.5.2 MTI models

This section presents the fundamentals of MTI state space models for which the definitions of tensor systems can be found in Pangalos et al. [35]. The MTI state space model in matrix representation of a state transition function is given by

$$\dot{\mathbf{x}} = \mathbf{F}\mathbf{m}(\mathbf{x}, \mathbf{u}), \tag{2.41}$$

with the transition matrix $\mathbf{F} \in \mathbb{R}^{n\times\beta}$, where $\beta = 2^{(n+m)}$, and the monomial vector $\mathbf{m}(\mathbf{x}, \mathbf{u})$ defined as

$$\mathbf{m}(\mathbf{x}, \mathbf{u}) = \begin{pmatrix} 1 \\ u_m \end{pmatrix} \otimes \cdots \otimes \begin{pmatrix} 1 \\ u_1 \end{pmatrix} \otimes \begin{pmatrix} 1 \\ x_n \end{pmatrix} \otimes \cdots \otimes \begin{pmatrix} 1 \\ x_1 \end{pmatrix}, \tag{2.42}$$

where $\otimes$ denotes the Kronecker product [36]. The state transition function can be translated into a state transition tensor system expressed in terms of the transition tensor and the monomial canonical polyadic (CP) tensor. In the following, the notation $\mathbb{R}^{\times^{(n+m)}2}$ will denote the space $\mathbb{R}^{\overbrace{2\times\cdots\times 2}^{n+m\; times}}$. The state transition function of a tensor system expressed as a contracted tensor product is

$$\dot{\mathbf{x}} = \langle\, \mathsf{F} \,|\, \mathsf{M}(\mathbf{x}, \mathbf{u}) \,\rangle\,, \tag{2.43}$$

with the state transition tensor $\mathsf{F} \in \mathbb{R}^{\times^{(n+m)}2\times n}$ and the monomial tensor

$$\mathsf{M}(\mathbf{x}, \mathbf{u}) = \left[\begin{pmatrix} 1 \\ u_m \end{pmatrix}, \cdots, \begin{pmatrix} 1 \\ u_1 \end{pmatrix}, \begin{pmatrix} 1 \\ x_n \end{pmatrix}, \cdots, \begin{pmatrix} 1 \\ x_1 \end{pmatrix}\right] \in \mathbb{R}^{\times^{(n+m)}2}. \tag{2.44}$$

Considering that contracted products can be efficiently computed in CP form, the decomposition of the state transition tensor

$$\mathsf{F} = [\mathbf{F}_{u_m}, \ldots, \mathbf{F}_{u_1}, \mathbf{F}_{x_n}, \ldots, \mathbf{F}_{x_1}, \mathbf{F}_{\Phi}] \cdot \lambda_f \tag{2.45}$$

is desired allowing to express the contracted product of the decomposed tensor in terms of single matrix operations

$$\langle \mathsf{F} \,|\, \mathsf{M}(\mathbf{x},\mathbf{u}) \rangle = \mathbf{F_\Phi}\left(\lambda_f \circledast \left(\mathbf{F}_u^\mathsf{T}\begin{pmatrix}1\\u\end{pmatrix}\right)\right) \circledast \cdots \circledast \left(\mathbf{F}_{x_2}^\mathsf{T}\begin{pmatrix}1\\x_2\end{pmatrix}\right) \circledast \left(\mathbf{F}_{x_1}^\mathsf{T}\begin{pmatrix}1\\x_1\end{pmatrix}\right), \tag{2.46}$$

with the Hamadard (elementwise) product denoted by $\circledast$.

Approximation of non-linear systems

To leverage the efficiency of computing contracted products, Kruppa et al. [36] present an approximation of the non-linear system in (2.34) based on

$$\dot{\mathbf{x}} = \langle \mathsf{F} \,|\, \mathsf{M}(\mathbf{x},\mathbf{u}) \rangle = \left(h_1(\mathbf{x},\mathbf{u}) \cdots h_n(\mathbf{x},\mathbf{u})\right)^\mathsf{T}, \tag{2.47}$$

with n states x and m inputs u. This approximation is valid for a certain operation range dictated by the given engineering application formally expressed as

$$x_i \in \left[x_{i,l}, x_{i,u}\right], i = 1, \dots, n, \tag{2.48}$$
$$u_j \in \left[u_{j,l}, u_{j,u}\right], j = 1, \dots, m. \tag{2.49}$$

The approximation functions $h_i(\mathbf{x},\mathbf{u})$ can be computet elementwise according to

$$h_j(\mathbf{x},\mathbf{u}) = \langle \mathsf{F} \,|\, \mathsf{M}(\mathbf{x},\mathbf{u}) \rangle\,(j) = \sum_{i=1}^{2^{n+m}} \varphi_{\mathsf{i}_i,j}\mu_{\mathsf{i}_i}(\mathbf{x},\mathbf{u}), \forall j = 1, \dots, n, \tag{2.50}$$

with the monomial tensor $\mathsf{M}(\mathbf{x},\mathbf{u})$ with scalar elements $\varphi_{\mathsf{i}_i,j}$ and the state transition tensor F with scalar elements μ_{i_i}.

2.6 PID control

The role of controllers in the dynamic operation of plants is essential, as they steer plants to achieve the desired behavior. Given its significance and widespread use in industrial applications, this thesis utilizes a PID controller. Figure 2.15 depicts the working principle of a PID controller based on classical feedback control. In this setup, the error e, which represents the comparison between the plant's output y and the reference r, is fed to the controller. The controller is responsible for providing a suitable plant input u to reduce the error e for the next time step.

The structure of such a PID controller relies on proportional K_p, integral K_i, and derivative K_d actions, all of which can be adjusted for continuous modulated control. The

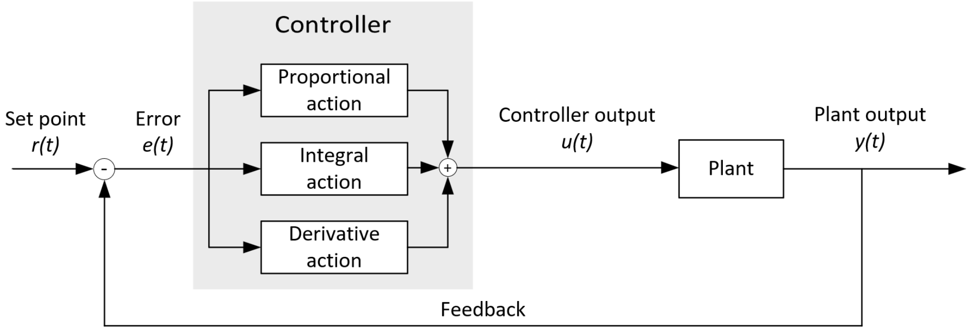

Figure 2.15: Feedback PID control
(Own figure based on [37]).

controller's output signal $u(t)$ is given by

$$u(t) = K_p\, e(t) + K_i \int_0^t e(\tau)\mathrm{d}\tau + K_d\, \frac{\mathrm{d}}{\mathrm{d}t} e(t). \tag{2.51}$$

Here, K_p applies proportional changes of the error to the controller output, K_i contributes reducing steady state errors through low frequency compensation, and K_d improves transient response through high frequency compensation [38].
Applying the Laplace transform to the controller output in the time domain, expresses it in the s domain as

$$U(s) = \left(K_p + K_i\, \frac{1}{s} + K_d\, s\right) E(s), \tag{2.52}$$

with $U(s)$ and $E(s)$ corresponding to the signals $u(t)$ and $e(t)$ in the time domain.
Practical PID controllers often include a low-pass filter N to process noisy signals of the error's derivative

$$U(s) = \left(K_p + K_i\, \frac{1}{s} + K_d \frac{sN}{s+N}\right) E(s). \tag{2.53}$$

2.7 Power consumption of pumps

Pumps are defined as turbomachines that impart energy to a liquid, typically by means of a rotating shaft, in order to transport it through pipe or duct systems. This increase in fluid energy usually results in a corresponding rise in fluid pressure, which is directly proportional to the pump's input power or brake horsepower

$$\dot{W}_{\mathrm{pump}} = \frac{\dot{v}\,(\Delta p_{\mathrm{pump}})}{\eta_{\mathrm{pump}}}, \tag{2.54}$$

with the liquid volume flow $\dot{v}$, the pressure increase across the pump Δp_{pump}, and the pump efficiency η_{pump} [39]. Here, η_{pump}, in a range from 0 to 1, accounts for irreversible losses caused by friction or internal leakage within the pump.

The pressure increase across the pump, Δp_{pump}, is determined by the energy needed to propel the liquid through its respective circuit. Consider the feed water or hot fluid circuit shown in Figure 2.4 to exemplify this concept's application. Here, the feed water pump is required to provide adequate energy to overcome the resistances that oppose the fluid flow in the piping network, the PHE, and the stack as it returns to the feed water tank. Figure 2.16 illustrates a block and a schematic fluid energy diagram relevant to this circuit.

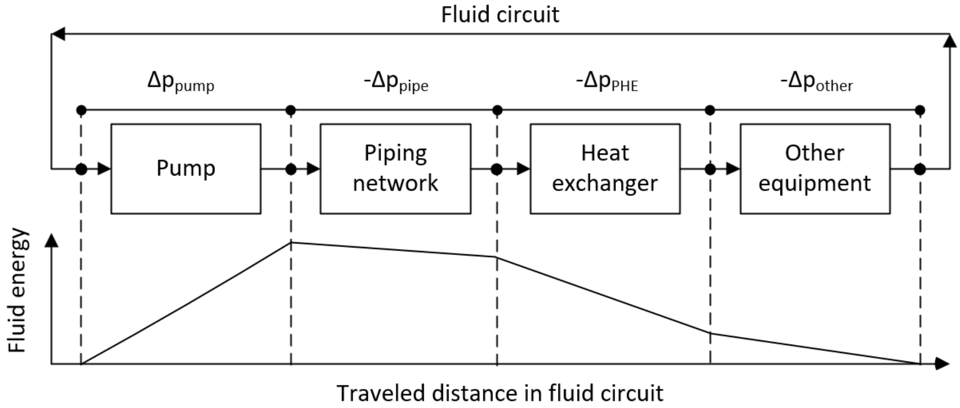

Figure 2.16: Fluid energy levels in pumping circuit.

From Çengel et al. [39], it follows that for a system with no fluid acceleration, the pressure increase in the feed water pump is given by

$$\Delta p_{\text{pump}} = \Delta p_{\text{pipe}} + \Delta p_{\text{PHE}} + \Delta p_{\text{other}}, \tag{2.55}$$

with the pressure drop in the piping system Δp_{pipe}, the pressure drop in the PHE Δp_{PHE}, and the pressure drop in other equipment Δp_{other}. In the case of the feed water circuit, Δp_{other} accounts for the pressure drop in the stack, while for the cooling water circuit, Δp_{other} accounts for pressure losses in the air cooler. In the following, the details for calculating the individual pressure losses in (2.55) are provided.

2.7.1 Pressure drop in round pipes

Pressure drop in round pipes can be calculated using the Darcy-Weisbach equation

$$\Delta p_{\text{pipe}} = \Delta \hat{p}_{\text{pipe}} L_{\text{eq}}, \tag{2.56}$$

with the pressure drop per unit of pipe length $\Delta \hat{p}_{\text{pipe}}$ and the pipe equivalent length L_{eq} [40]. Here, $\Delta \hat{p}_{\text{pipe}}$ is given by

$$\Delta \hat{p}_{\text{pipe}} = 8.1039 \times 10^{11} \frac{f(\dot{m})^2}{d^5 \rho}, \tag{2.57}$$

with the pipe diameter d, and the pipe friction factor f [41]. The Churchill equation allows calculation of the pipe friction factor spanning all fluid regimes using

$$\frac{f}{8} = \left[\left(\frac{8}{Re}\right)^{12} + \frac{1}{(\Theta_1 + \Theta_2)^{1.5}}\right]^{\frac{1}{12}}, \tag{2.58}$$

where

$$\Theta_1 = \left[-2.457 \ln\left(\left(\frac{7}{Re}\right)^{0.9} + 0.27\frac{\epsilon}{d}\right)\right]^{16}, \tag{2.59}$$

$$\Theta_2 = \left(\frac{37530}{Re}\right)^{16}, \tag{2.60}$$

with the pipe Reynolds number Re, and the pipe roughness factor ϵ.

The pipe equivalent length L_{eq} in (2.56) corresponds to the actual pipe length plus the pipe equivalent length associated with the frictional resistance of all fittings (e.g., 90-degree elbows, flanges, tees) and valves in the piping network. In cases where detailed pipe design is unknown, the pipe equivalent length can be estimated using

$$\frac{L_{\mathrm{eq}}}{L} = 1 + (0.347 d^{1/2} + 0.216) F_c, \tag{2.61}$$

with the actual pipe length L and the complexity factor F_c [42]. The complexity factor depends upon the type of piping network according to:

- $F_c = 4$ for very complex manifolds
- $F_c = 2$ for manifold type piping
- $F_c = 1$ normal piping
- $F_c = 0.5$ for long straight pipe run

The pipe diameter d can be estimated considering practical flow velocity in pipelines, which should be at least 0.9 $\mathrm{m\,s^{-1}}$ [43]. A typical interval for the flow velocity of non-viscous liquids in pipelines is $1.0\,\mathrm{m\,s^{-1}}$ to $3.0\,\mathrm{m\,s^{-1}}$ [44].

2.7.2 Pressure drop in PHE

The pressure drop in a PHE is expressed as a sum of the individual contributions

$$\Delta p_{\mathrm{PHE}} = \Delta p_{\mathrm{PHE,ch}} + \Delta p_{\mathrm{PHE,po}}, \tag{2.62}$$

with the frictional channel pressure drop $\Delta p_{\text{PHE,ch}}$ and the port pressure drop $\Delta p_{\text{PHE,po}}$ in the PHE. The frictional channel pressure drop can be calculated using

$$\Delta p_{\text{PHE,ch}} = 4\, f_{\text{ch}} \frac{L_v n_{\text{p}}}{d_{\text{ch}}} \frac{G_{\text{ch}}^2}{2\rho} \left(\frac{\mu}{\mu_w} \right)^{-0.17}, \tag{2.63}$$

with the plate vertical length between ports L_v, the number of passes n_{p}, and the channel friction factor f_{ch} [18]. The calculation of the channel friction factor f_{ch} is given by (2.29). For the port pressure drop holds

$$\Delta p_{\text{PHE,po}} = 1.4\, n_{\text{p}} \frac{G_{\text{po}}^2}{2\rho} \tag{2.64}$$

with the port mass velocity G_{po} equal to

$$G_{\text{po}} = \frac{\dot{m}}{\pi d_{\text{po}}^2}, \tag{2.65}$$

where the port diameter d_{po} is used for its calculation.

2.7.3 Pressure drop in other equipment

As depicted in Figure 2.4 and 2.16, Δp_{other} represents the pressure drop attributable to the stack in the feed water circuit and the air cooler in the cooling water circuit. Although there have been studies on the flow characteristics of feed water circulating through the stacks in PEM electrolyzers [45–48], there are no general correlations or collected data for pressure drop analysis in electrolyzers on the MW scale. Therefore, subsection 3.6.2 presents a conservative assumption for the pressure drop across the PEM stack for hydraulic analysis. Regarding the cooling water circuit, considering the typical construction bundle of tube sheet plus header for air coolers [49], the related pressure drop aligns with the typical tube side pressure drop in shell and tube HEs, 62 kPa [50].

3 Model definitions and structure

This chapter presents a detailed overview of the 1 MW electrolyzer model developed using MATLAB and SIMULINK. The chapter starts with a thorough examination of the structure of the 1 MW electrolyzer base model and its essential components to introduce the description of the enhanced model structure developed in this thesis. In addition, the chapter outlines the fundamental premises for the PHE sizing and its first principles (FP) modeling. This is followed by the framework for implementation of the LTI and MTI modeling approaches and the PID controller design. Finally, the chapter presents an overview of the system's configuration, with a specific focus on estimating pump power consumption.

3.1 Electrolyzer base model

The non-linear 1 MW PEM electrolyzer base model is a thermal dynamic and electric static model scaled up from a reference 46 kW electrolyzer available in Espinosa-López et al. [9]. Table 3.1 provides a summary of the reference and base or scaled-up parameters for the 1 MW electrolyzer model, which is based on the following assumptions:

- Negligible cathode activation losses
- Negligible mass transfer losses
- Ideal gas behavior of non-condensed phases
- No water evaporation

The electrolyzer's thermal model consists of a lumped thermal capacitance model [9]

$$C_{\mathrm{th}}\frac{\mathrm{d}T}{\mathrm{d}t} = \dot{W}_{\mathrm{stack,heat}} + \dot{W}_{\mathrm{pump,heat}} - \dot{Q}_{\mathrm{cool}} - \dot{Q}_{\mathrm{loss}} - \dot{H}_{\mathrm{H_2}} - \dot{H}_{\mathrm{O_2}}, \tag{3.1}$$

with the thermal capacity of the water inside the control volume C_{th}, the energy loss released as heat by the stack $\dot{W}_{\mathrm{stack,heat}}$, the power losses converted into heat at the feed water pump $\dot{W}_{\mathrm{pump,heat}}$, the cooling load extracted by the cooling or secondary water

Table 3.1: Parameters of of 1 MW electrolyzer base model.

Property	Initial	Base or scaled-up	Comment
Nominal load (kW)	46	1	
Nominal temperature (°C)	60	60	
Nominal cathode pressure (bar)	30	30	
Current density at nom. current ($\mathrm{A\,cm^{-2}}$)	1.485	1.485	at P_{nom}
Cell voltage at nom. current (V)	1.780	1.780	at P_{nom}
Cell surface ($\mathrm{cm^2}$)	290	5000	
Number of cells	60	75	
Electrolyzer nominal voltage (V)	106.8	133.5	$n_{\text{cells}}\,V_{\text{cell}}$
Lumped thermal capacity ($\mathrm{J\,K^{-1}}$)	1.621×10^6	3.494×10^6	Scaled-up by volume
Thermal resistance ($\mathrm{K\,W^{-1}}$)	0.0668	0.0031	Scaled-up by power
Feed water flow ($\mathrm{L\,min^{-1}}$)	140	3017	Scaled-up by volume
Pump power (kW)	1.1	23.7	Scaled-up by volume

loop $\dot{Q}_{\text{cool}}$, the heat losses released to the ambient $\dot{Q}_{\text{loss}}$ and the energy leaving the system in the hydrogen and oxygen streams, $\dot{H}_{\text{H}_2}$ and $\dot{H}_{\text{O}_2}$. This thesis focuses on analyzing the cooling system, specifically the model structure for calculating $\dot{Q}_{\text{cool}}$.

The cooling system comprises a PID controller with the error signal e as input and the cooling load $\dot{Q}_{\text{cool}}$ to the electrolyzer as output, as depicted in Figure 3.1. It is important to note that this cooling system structure differs significantly from a real system as it does not include a final control element that can be physically adjusted to maintain the desired temperature levels in the stack.

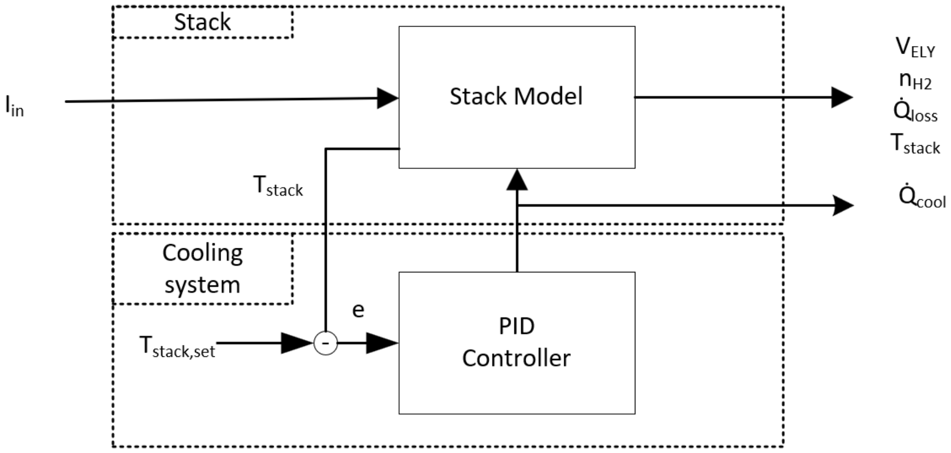

Figure 3.1: Structure of the 1 MW electrolyzer base model.

3.2 Electrolyzer updated model

For the parameters in Table 3.1 a new relationship for calculating the feed water flow is introduced based in (2.3)

$$\dot{v}_{\mathrm{H_2O}} = \frac{n_{\mathrm{cell}} I}{2F} \frac{1080}{\rho_{\mathrm{H_2O}} F_e}, \tag{3.2}$$

with the feed water volume flow $\dot{v}_{\mathrm{H_2O}}$ in $\mathrm{L\,min^{-1}}$, and the excess water flow factor F_e defined as

$$F_e = \frac{\dot{v}_{\mathrm{H_2O,min}}}{\dot{v}_{\mathrm{H_2O}}}. \tag{3.3}$$

The excess water flow factor F_e is introduced to account for the excess flow required to avoid overheating of the electrolysis stack as shown in section 2.1. For calculation of $\dot{v}_{\mathrm{H_2O}}$ in (3.2), I corresponds to the current at electrolyzer's nominal load, and F_e is set to 0.35×10^{-2} to keep the relationship in the reference 46 kW electrolyzer model. Table 3.2 presents the parameters for the updated model compared to the base model.

Table 3.2: Parameters of 1 MW electrolyzer updated model.

Value	Base or scaled-up model	Updated model
Feed water flow ($\mathrm{L\,min^{-1}}$)	3017	910

The updated 1 MW electrolyzer model includes new components, such as a PHE model in the cooling system, a PID controller, and a sub-module to calculate $\dot{Q}_{\mathrm{cool}}$. This model structure closely resembles a real system relying on a PHE. The output of the new PID controller is a signal for the cooling water volumetric flow, $\dot{v}_{\mathrm{c}}$, which can be utilized to regulate a physical device, such as the power input to the cooling water pump, in order to steer the system to the desired condition. Figure 3.2 illustrates the updated structure for the cooling system and its integration with the stack model. In testing and analyzing this enhanced 1 MW electrolyzer model, the following premises are considered:

- Simulations are carried out over one week using a variable power profile.
- The stack power input, P_{stack}, is set within a range from P_{min} to P_{nom}, with $P_{\mathrm{nom}} = 1$ MW and $P_{\mathrm{min}} = 0.2\,P_{\mathrm{nom}}$. This range is chosen to cover the electrolyzer's various operating conditions.
- Scenarios of the electrolyzer's cold start or cooling down are not investigated.
- The model is tailored to size the cooling system at the maximum waste heat rate in the stack, $\dot{W}_{\mathrm{stack,heat}}$, which corresponds to the electrolyzer operating at nominal load and end of life (EoL) state.
- Throughout the simulations, the volume flow of feed water, $\dot{v}_{\mathrm{h}}$, is kept constant.

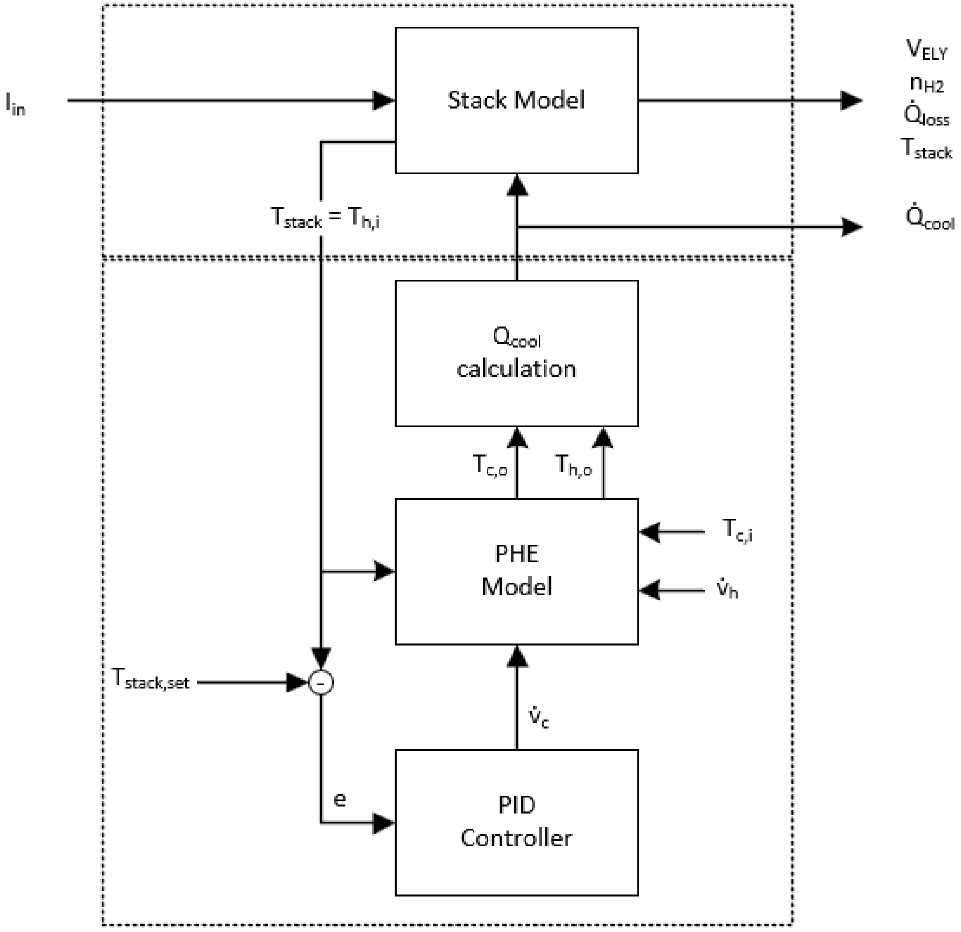
I_in
Stack Model
V_ELY
n_H2
Q̇_loss
T_stack
T_stack = T_h,i
Q̇_cool
Q_cool calculation
T_c,o
T_h,o
PHE Model
T_c,i
V̇_h
T_stack,set
-
V̇_c
e
PID Controller

Figure 3.2: Structure of the 1 MW electrolyzer updated model.

- The PHE sizing is based on plates with properties detailed in Table 3.3.

- The PHE is sized to guarantee a maximum temperature difference of 10 °C between the stack inlet temperature ($= T_{\mathrm{h,o}}$) and the stack's outlet temperature ($\approx T_{\mathrm{h,i}}$) at maximum cooling water flow.

- The air cooler in the cooling water circuit maintains a constant PHE inlet temperature of the cooling water, $T_{\mathrm{c,i}} = 30$ °C.

- For stack temperature control, $T_{\mathrm{stack,set}}$ is equal to 60 °C.

This updated structure requires a PHE model, the design of which is elaborated in the following section.

3.3 PHE sizing and FP modeling

The design of PHE is derived from the energy balances and heat transfer relationships detailed in section 2.2. In order to fully characterize the heat transfer process, fluid properties such as density ρ, specific heat c_p, and the overall heat transfer coefficient U are necessary and vary with temperature, as indicated in (2.5), (2.6) and (2.8). To optimize simulation time, an approach using constant properties at average temperature and fluid conditions is investigated to avoid recalculating these properties as the temperature changes during dynamic simulations. The findings are presented in section A.1, demonstrating the viability of using average values for the fluid properties and the heat transfer coefficient. For water-water systems, the range of U falls between $3000\,\mathrm{W\,m^{-2}\,K^{-1}}$ to $7000\,\mathrm{W\,m^{-2}\,K^{-1}}$ [18].

Combination of (2.5), (2.6) and (2.7) using average values for temperature dependent properties delivers the FP model of the PHE used in this thesis

$$\left(\bar{\rho}_{\mathrm{h}} v_{\mathrm{HU_h}} \bar{c}_{p_{\mathrm{h}}}\right) \frac{\mathrm{d}T_{\mathrm{h,o}}}{\mathrm{d}t} = \dot{v}_{\mathrm{h}} \bar{\rho}_{\mathrm{h}} \bar{c}_{p_{\mathrm{h}}} \left(T_{\mathrm{h,i}} - T_{\mathrm{h,o}}\right) - \bar{U} A \frac{\left(T_{\mathrm{h,i}} - T_{\mathrm{c,o}}\right) - \left(T_{\mathrm{h,o}} - T_{\mathrm{c,i}}\right)}{\ln\left(\frac{T_{\mathrm{h,i}} - T_{\mathrm{c,o}}}{T_{\mathrm{h,o}} - T_{\mathrm{c,i}}}\right)}, \tag{3.4}$$

$$\left(\bar{\rho}_{\mathrm{c}} v_{\mathrm{HU_c}} \bar{c}_{p_{\mathrm{c}}}\right) \frac{\mathrm{d}T_{\mathrm{c,o}}}{\mathrm{d}t} = \dot{v}_{\mathrm{c}} \bar{\rho}_{\mathrm{c}} \bar{c}_{p_{\mathrm{c}}} \left(T_{\mathrm{c,i}} - T_{\mathrm{c,o}}\right) + \bar{U} A \frac{\left(T_{\mathrm{h,i}} - T_{\mathrm{c,o}}\right) - \left(T_{\mathrm{h,o}} - T_{\mathrm{c,i}}\right)}{\ln\left(\frac{T_{\mathrm{h,i}} - T_{\mathrm{c,o}}}{T_{\mathrm{h,o}} - T_{\mathrm{c,i}}}\right)}. \tag{3.5}$$

where the total heat transfer area A is unknown motivating the design of the PHE to enable the computation of fluid energy balances.

The PHE design involves determining the size of the heat exchanger, specifically its total transfer area, reflected on the number of selected plates. The design case for sizing the PHE is based on the electrolyzer operating at its nominal load, leading to the maximum heat loss rate in the stack as shown in (2.2). This corresponds to the maximum required heat transfer area considering its proportionally to the cooling heat transfer rate according to (2.7). The total heat transfer area A of the PHE can be calculated as

$$A = n_{\mathrm{plate}} A_{\mathrm{plate,e}}, \tag{3.6}$$

with the number of plates n_{plate}. Here, $A_{\mathrm{plate,e}}$ is calculated based on the plate geometry outlined in Table 3.3 The number of plates n_{plate} is determined using the ceiling function, rounding up to the nearest integer to obtain a discrete number of plates for the PHE given by

$$n_{\mathrm{plate}} = \left\lceil \frac{A_{\mathrm{theoretical}}}{A_{\mathrm{plate,e}}} \right\rceil, \tag{3.7}$$

where $A_{\mathrm{theoretical}}$ is calculated using the following procedure:

1. Calculate $T_{\mathrm{h,o}}$ based on $\dot{v}_{\mathrm{h}}$, $T_{\mathrm{h,i}}$, and the required $\dot{Q}_{cool}$.

Table 3.3: PHE plates characteristics [18].

Property	Value
Plate material	SS304
Plate thickness, δ_{plate}	0.6×10^{-3} m
Chevron angle, β	$45°$
Enlargement factor,ϕ	1.25
Plate effective heat transfer area (m^2)	1.07
Plate projected area (m^2)	0.85
Ports diameter, d_{po}	0.2 m
Ports vertical distance, L_{v}	1.55 m
Ports horizontal distance, L_{h}	0.43 m
Plate width inside gaskets, L_{w}	0.63 m
Plate thermal conductivity, k_{plate}	17.5 $\text{Wm}^{-1}\text{K}^{-1}$

2. Set the value for $T_{\text{c,i}}$ in the cooling water system.
3. Choose a value for $T_{\text{c,o}}$ such that $T_{\text{c,o}} < T_{\text{h,i}}$.
4. Calculate the density ρ and the specific heat capacity c_p at mean temperature for the hot and cold fluid according to $T_{\text{m}} = (T_{\text{i}} + T_{\text{o}})/2$.
5. Calculate the heat transfer rate $\dot{Q}$ and the heat capacity rates C_{c} and C_{h} with (2.17).
6. Calculate the ratio of heat capacity rates C^* and the PHE effectiveness ε with (2.15) and (2.19).
7. Calculate the number of transfer units NTU using (2.23).
8. Verify: If $2.0 < \text{NTU} < 3.0$, then finish. If not, return to step 3.

The calculation of A rounds up the sizing procedure for PHE, allowing the implementation and dynamic analysis of its FP model. The following section presents alternative LTI and MTI model approaches for further study.

3.4 PHE modeling approaches

The model structure used to generate the LTI and MTI models is based on the FP formulation in (3.4) to (3.5) written in the form of (2.34) delivering

$$\frac{\mathrm{d}T_{\text{h,o}}}{\mathrm{d}t} = \frac{1}{\bar{\rho}_{\text{h}} v_{\text{HU}_\text{h}} \bar{c}_{p_\text{h}}} \left(\dot{v}_{\text{h}} \bar{\rho}_{\text{h}} \bar{c}_{p_\text{h}} \left(T_{\text{h,i}} - T_{\text{h,o}}\right) - \bar{U} A \frac{(T_{\text{h,i}} - T_{\text{c,o}}) - (T_{\text{h,o}} - T_{\text{c,i}})}{\ln\left(\frac{T_{\text{h,i}} - T_{\text{c,o}}}{T_{\text{h,o}} - T_{\text{c,i}}}\right)} \right), \tag{3.8}$$

$$\frac{\mathrm{d}T_{\text{c,o}}}{\mathrm{d}t} = \frac{1}{\bar{\rho}_{\text{c}} v_{\text{HU}_\text{c}} \bar{c}_{p_\text{c}}} \left(\dot{v}_{\text{c}} \bar{\rho}_{\text{c}} \bar{c}_{p_\text{c}} \left(T_{\text{c,i}} - T_{\text{c,o}}\right) + \bar{U} A \frac{(T_{\text{h,i}} - T_{\text{c,o}}) - (T_{\text{h,o}} - T_{\text{c,i}})}{\ln\left(\frac{T_{\text{h,i}} - T_{\text{c,o}}}{T_{\text{h,o}} - T_{\text{c,i}}}\right)} \right), \tag{3.9}$$

with the two states $\mathbf{x}$, and four inputs $\mathbf{u}$

$$\mathbf{x} = \begin{pmatrix} x_1 & x_2 \end{pmatrix}^\mathsf{T} = \begin{pmatrix} T_{\mathrm{h,o}} & T_{\mathrm{c,o}} \end{pmatrix}^\mathsf{T} \tag{3.10}$$

$$\mathbf{u} = \begin{pmatrix} u_1 & u_2 & u_3 & u_4 \end{pmatrix}^\mathsf{T} = \begin{pmatrix} \dot{v}_{\mathrm{h}} & \dot{v}_{\mathrm{c}} & T_{\mathrm{h,i}} & T_{\mathrm{c,i}} \end{pmatrix}^\mathsf{T} \tag{3.11}$$

In order to facilitate later comparison of the models, it is essential to establish the benchmark design case where the electrolyzer operates at nominal load. The cooling load associated with this design case corresponds directly to the following inputs

$$\mathbf{u} = \begin{pmatrix} \dot{v}_{\mathrm{h}} \\ \dot{v}_{\mathrm{c}} \\ T_{\mathrm{h,i}} \\ T_{\mathrm{c,i}} \end{pmatrix} = \begin{pmatrix} 909\ \mathrm{L\,min^{-1}} \\ 202\ \mathrm{L\,min^{-1}} \\ 60\ °\mathrm{C} \\ 30\ °\mathrm{C} \end{pmatrix}. \tag{3.12}$$

In this case, the inlet temperatures of hot and cold fluid are used as initial values for the states

$$\mathbf{x_0} = \begin{pmatrix} T_{0,\mathrm{h,o}} \\ T_{0,\mathrm{c,o}} \end{pmatrix} = \begin{pmatrix} T_{\mathrm{h,i}} \\ T_{\mathrm{c,i}} \end{pmatrix} = \begin{pmatrix} 60\ °\mathrm{C} \\ 30\ °\mathrm{C} \end{pmatrix}, \tag{3.13}$$

achieving the steady state

$$\tilde{\mathbf{x}} = \begin{pmatrix} \tilde{T}_{\mathrm{h,o}} \\ \tilde{T}_{\mathrm{c,o}} \end{pmatrix} = \begin{pmatrix} 55\ °\mathrm{C} \\ 56\ °\mathrm{C} \end{pmatrix}. \tag{3.14}$$

3.4.1 LTI modeling

A linear approximation of (3.8) and (3.9) around the steady state of the design case is computed using the MATLAB function *linmod* to obtain the matrices in (2.39). The steady-state condition is computed using the MATLAB function *trim*.

3.4.2 MTI modeling

The multilinear approximation of the FP model uses the multilinearization method introduced by Kruppa et al. [36]. The numerical implementation was performed using the MTI Toolbox [51] and the Sparse Grids Matlab Kit [52]. In this application, specific operating ranges for states and inputs have been defined as

$$T_{\mathrm{h,o}} \in [50\ ^\circ\mathrm{C},\ 65\ ^\circ\mathrm{C}]\,, \tag{3.15}$$

$$T_{\mathrm{c,o}} \in [40\ ^\circ\mathrm{C},\ 60\ ^\circ\mathrm{C}]\,, \tag{3.16}$$

$$\dot{v}_{\mathrm{h}} \in \left[180\ \mathrm{L\,min^{-1}},\ 910\ \mathrm{L\,min^{-1}}\right]\,, \tag{3.17}$$

$$\dot{v}_{\mathrm{c}} \in \left[0\ \mathrm{L\,min^{-1}},\ 800\ \mathrm{L\,min^{-1}}\right]\,, \tag{3.18}$$

$$T_{\mathrm{h,i}} \in [55\ ^\circ\mathrm{C},\ 65\ ^\circ\mathrm{C}]\,, \tag{3.19}$$

$$T_{\mathrm{c,i}} \in [25\ ^\circ\mathrm{C},\ 35\ ^\circ\mathrm{C}]\,. \tag{3.20}$$

Incorporating these intervals into the multilinearization algorithm yields a state transition function of the form in (2.47).

3.5 PID Controller

The PID controller used in the Simulink 1 MW electrolyzer model is implemented with the *PID Controller* block with one degree of freedom. The decision to use a PID controller rather than a PI or PD controller is made to increase the likelihood of meeting the design objectives without sacrificing robustness. This is due to the capability to tune three parameters: the proportional, integral, and derivative actions.

The PID controller is tuned using the PID Tuner app from the MATLAB Control System Toolbox, which utilizes an autotune algorithm requiring a linear model of the plant estimated around a selected operating point. In this context, the operating point for linearization corresponds to a steady-state condition.

The PID autotuning algorithm is used to find suitable PID parameters for the plant, using either the PHE FP or PHE MTI model, to compare their performances. In cases where the autotuning fails to deliver suitable PID parameters for the design objectives, manual adjustments are made to the target performance parameters for response time and transient behavior in order to achieve the desired results (Figure 3.3). This manual tuning involves a trial-and-error procedure in the time domain. For the set up and tuning of the PID controller, the following premises are considered:

- The PID controller design focuses on a balanced approach between reference tracking and input disturbance rejection.

- The PID controller incorporates a back-calculation anti-windup method using the default back-calculation coefficient in MATLAB.

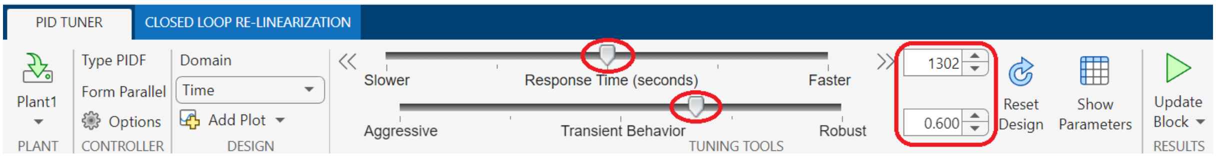
PID TUNER
CLOSED LOOP RE-LINEARIZATION
Plant1
PLANT
Options
CONTROLLER
Add Plot
DESIGN
Slower
Response Time (seconds)
Faster
Aggressive
Transient Behavior
Robust
TUNING TOOLS
Reset Design
Show Parameters
Update Block
RESULTS

Type PIDF
Form Parallel
Domain Time
1302
0.600

Figure 3.3: Target performance parameters in the MATLAB PID Tuner App.

3.6 Estimation of pump power consumption

In section 2.7, the pump's power consumption is dependent on the calculation of ΔP_{pump}, which is influenced by the pressure drop in the pipe routing, the PHE, and other equipment. The sizing of the PHE contains all the essential data needed to calculate the pressure drop, obviating the need for additional assumptions. This section delivers details of the considerations and assumptions associated with pipe routing and other equipment in the hot and cold fluid circuits.

3.6.1 Pressure drop in piping network

Since the specific pipe routing for the 1 MW electrolyzer is not available, the actual pipe length L in (2.61) is determined based on a 1.25 MW containerized electrolyzer [14] with available specifications and a 3D model. It is premised that the 1 MW electrolyzer also comprises a unit in a container of the same size as the 1.25 MW reference electrolyzer. Table 3.4 outlines the container dimensions of the electrolyzer, which are utilized to estimate the actual pipe length for the hot and cold fluid circuits based on the 3D model of the reference electrolyzer.

Table 3.4: Container dimensions for 1 MW electrolyzer [14].

Dimension	Value
Length (m)	12.2
Width (m)	2.5
Height (m)	3.0

The pipe diameters for the circuits are calculated, and standard sizes are chosen to ensure adequate fluid velocity in line with the guidelines in subsection 2.7.1. Moreover, a complexity factor F_c of one is taken into account for this type of piping network. The pipe routing dimensions for the 1 MW electrolyzer are detailed in Table 3.5.

Table 3.5: Pipe routing geometry.

Circuit	$L\,(\mathrm{m})$	$d\,(\mathrm{mm})$
Hot fluid	30.0	97.18
Cold fluid	30.0	49.22

3.6.2 Pressure drop in other equipment

The specific pressure drop correlation for the stack in the hot fluid circuit is currently unknown. As a result, a $\Delta p_{\mathrm{other}}$ of 200 kPa is assumed based on the pump head for the system analysed by Espinosa-López et al. [9]. It is assumed that $\Delta p_{\mathrm{other}}$ remains constant as the hot fluid mass flow rate, $\dot{v}_{\mathrm{h}}$, is constant.

In the cold fluid circuit, the pressure drop is dependent on the cold fluid flow, which is set by the PID controller. To address this, a curve fitting for the function $\Delta p_{\mathrm{other,c}} = f(\dot{m}_{\mathrm{c}})$ is performed using a second-degree polynomial, taking into consideration the quadratic relationship between pressure drop and fluid flow outlined in (2.57). The fitting points are chosen based on the pressure drop guideline of 62 kPa presented in subsection 2.7.3 and the required cold fluid flow at the design case.

4 Simulation results and discussion

The simulation results are presented in several sections in the upcoming chapter. These sections cover the thermal sizing of the PHE and provide a comparative performance analysis of PHE models in a standalone environment and a plant environment connected to the PID controller. Finally, the power consumption assessment results of the BOP components associated with the electrolyzer's cooling system are presented.

4.1 PHE sizing

The PHE is dimensioned for the specified design scenario using the methodology outlined in section 3.3. This yields a PHE with the dimensions and heat transfer characteristics detailed in Table 4.1. The sizing of the PHE is predicated on the fluid properties that represent the design scenario at the electrolyzer's nominal load (Table 4.2), with the cooling water flow rate being approximately 22 % of the feed water flow rate.

Table 4.1: PHE properties and thermal performance indicators.

PHE geometry	Value
Number of plates	9
Number of effective plates	7
Number of passes	1
Number of channel per pass	4
Mean plate channel gap (m)	3.4×10^{-3}
Plate pitch (m)	4.05×10^{-3}
PHE thermal performance	
Overall heat transfer coefficient ($\mathrm{W\,m^{-2}\,K^{-1}}$)	4000
Heat capacity rate ratio	0.21
Effectiveness	0.86
NTU	2.27

The PHE operates at the design condition depicted in Figure 4.1, with the maximum required cooling water flow. Consequently, a reduction in electrolyzer load will decrease the required cooling water flow, leading operating points with higher effectiveness.

Table 4.2: Stream properties for PHE sizing.

Property	Hot fluid	Cold fluid
Mass flow ($\mathrm{kg\,s^{-1}}$)	14.9	3.4
Inlet temperature (°C)	60.0	30.0
Outlet temperature (°C)	54.5	55.9
Specific heat capacity ($\mathrm{J\,kg^{-1}\,K^{-1}}$)	4180	3828
Density ($\mathrm{kg\,m^{-3}}$)	982	1023

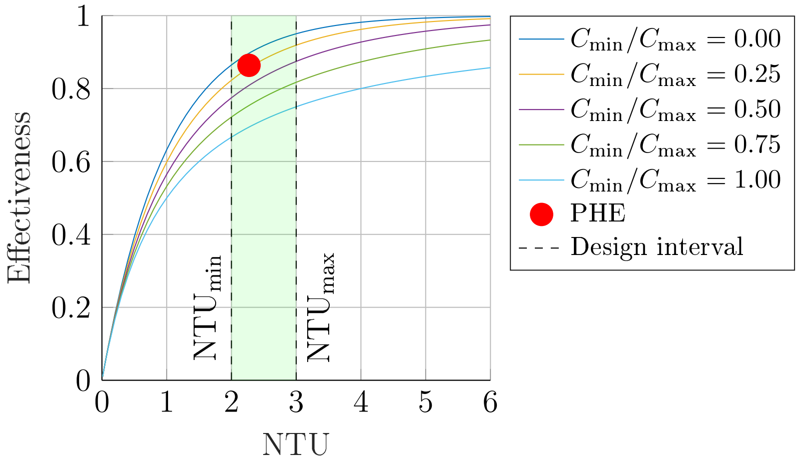

Figure 4.1: Thermal performance of the sized PHE.

4.2 PHE models comparison

In the examination and testing of the PHE model, the FP, LTI, and MTI approaches are employed for the design case. Figure 4.2 illustrates the transient and steady-state behavior of the model when subjected to the inputs described in (3.12) and the initial states outlined in (3.14). In Figure 4.2, the FP model is used as a benchmark for comparison, reaching its steady state at 15.4 s. The LTI model effectively replicates the steady state

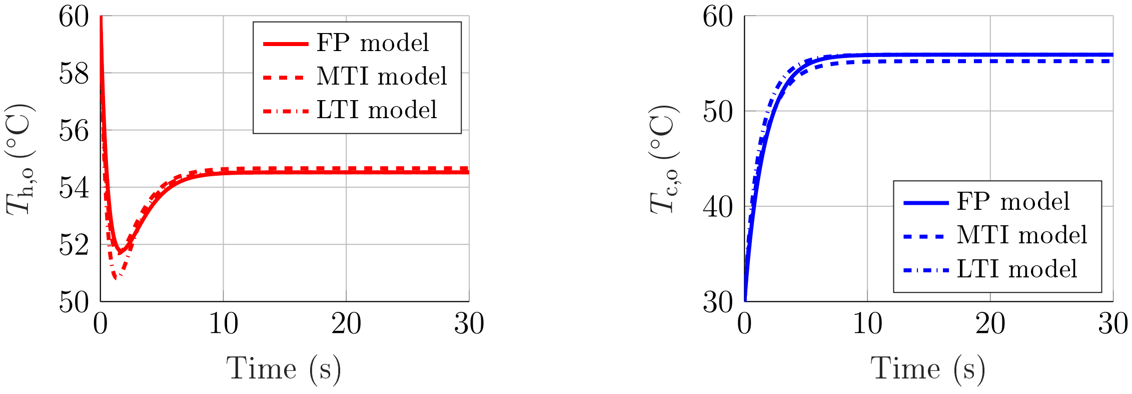

(a) Hot temperature profile

(b) Cold temperature profile

Figure 4.2: PHE models performance at design case scenario.

for both the hot fluid (Figure 4.2a) and the cold fluid (Figure 4.2b), as this steady-state condition is the input for the model linearization. During the transient period, the hot fluid temperature profile shows a maximum deviation of 1 °C, while the cold fluid profile deviates by 1.8 °C. On the other hand, the MTI model exhibits an offset when predicting the steady-state conditions, with a 0.14 °C offset for the hot fluid and a -0.67 °C offset for the cold fluid. However, it consistently outperforms the LTI model for both fluids' temperature profiles during the transient period.

Considering that the PHE model is to be fed with a variable cold fluid flow signal sent by the PID controller (Figure 3.2), further testing of the FP, LTI, and MTI modeling approaches is carried out with a variable $\dot{v}_c$ as shown in Figure 4.3.

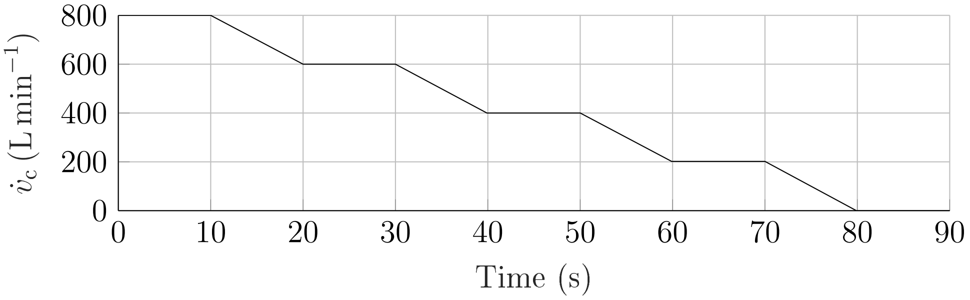

(a) Ramped down signal of cold fluid flow

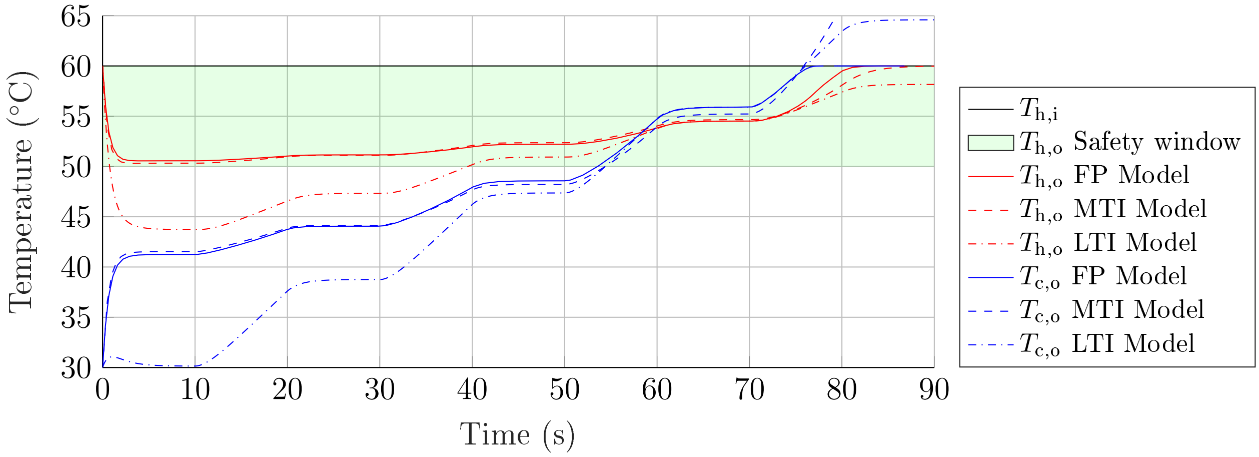

(b) PHE temperature profiles

Figure 4.3: PHE models performance with variable cold fluid flow.

For this test, a ramped-down signal covering the operating interval from 0 L min^{-1} to 800 L min^{-1} for $\dot{v}_c$ is used, encompassing the design case scenario $\dot{v}_c = 202$ L min^{-1} (Figure 4.3a). In Figure 4.3b, the electrolyzer's safe operational window indicates that the operation is safe, avoiding excessive mechanical stress due to the temperature difference when the hot fluid outlet temperature profile falls within this window.

On the one hand, the LTI model poorly reproduces the temperature profiles of the FP model at high $\dot{v}_c$. It exhibits deviations higher than 5 °C and 10 °C for the hot and cold fluid, respectively. These deviations pose a significant limitation for the extended use of the LTI model, as it inaccurately predicts hot fluid temperature profiles outside the electrolyzer safety window. Consequently, the LTI modeling approach is unsuitable for this application.

On the other hand, the MTI model accurately replicates the dynamic behavior of the FP model for $\dot{v}_c$ between $78\,\mathrm{L\,min^{-1}}$ and $800\,\mathrm{L\,min^{-1}}$. However, it fails to replicate the asymptotic behavior of $T_{c,o}$ towards $T_{h,i}$ when $\dot{v}_c$ is around $78\,\mathrm{L\,min^{-1}}$, resulting in the prediction of $T_{c,o} > T_{h,i}$ (Figure 4.4), which is not achievable by the PHE according to the system's thermodynamics. Therefore, the MTI model should not be used for $\dot{v}_c < 78\,\mathrm{L\,min^{-1}}$.

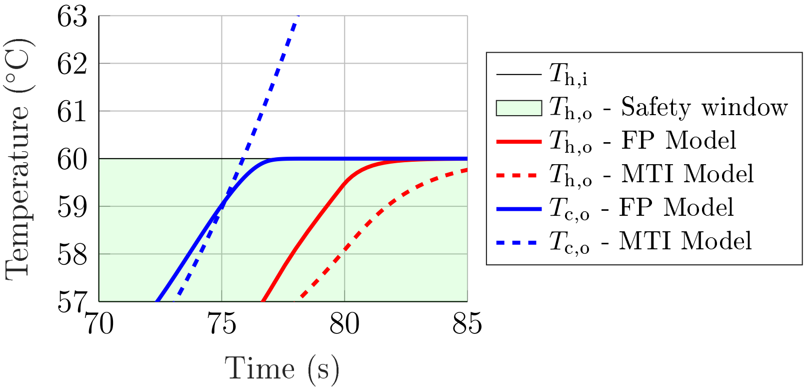

Figure 4.4: PHE FP and MTI model performance at low cold fluid flow.

4.3 PID controller perfomance

For the forthcoming analysis, the electrolyzer model should be regarded as a combination of a plant and a PID controller, as depicted in Figure 2.15. In this context, the plant comprises all blocks in the control loop except for the PID controller itself. This means the plant includes the stack, PHE model, and the $\dot{Q}_{cool}$ calculation block in Figure 3.2. The electrolyzer model is then evaluated using the stack power input curve displayed in Figure 4.5. The tuning of the PID controller involves the use of both manual and autotuning tools within the MATLAB PID Tuner app. Table 4.3 summarizes the various combinations of plants employed for tuning and simulation.

Table 4.3: Controllers tested in electrolyzer model.

		PHE model in plant for	
ID	Tuning method	tuning	simulation
Controller 1	Autotuning	FP model	FP model
Controller 2	Autotuning	FP model	MTI model
Controller 3	Autotuning	MTI model	MTI model
Controller 4	Trial and error	MTI model	MTI model

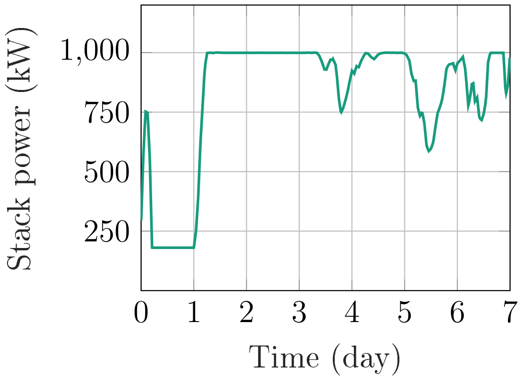

Figure 4.5: Stack power input curve.

4.3.1 Plant with PHE FP model

The plant's controller setup using the PHE FP model has output signal saturation limits for $\dot{v}_\mathrm{c}$ between 0 $\mathrm{L\,min^{-1}}$ and 800 $\mathrm{L\,min^{-1}}$, aligning with the operating interval defined in subsection 3.4.2. The plant dynamics using the PHE FP model indicate a steady state operating point at 2.32 day, which corresponds to the electrolyzer operating at a nominal load (Figure 4.5). The plant linearization is performed at 2.32 day. The parameters for the autotuned PID controller, referred to as Controller 1, are outlined in Table 4.4.

Table 4.4: Set up and performance parameters of Controller 1.

Property	Value
Proportional action, K_p	15.30
Integral action, K_i	0.11
Derivative action, K_d	-117.44
Filter coefficient, N	0.0114
Saturation lower limit (L $\mathrm{min^{-1}}$)	0
Saturation upper limit (L $\mathrm{min^{-1}}$)	800
Initial value (L $\mathrm{min^{-1}}$)	130

(a) Set up parameters

Target perfomance parameters	Value
Response time (s)	299.5
Transient behavior	0.6
Performance and robustness indicators	
Rise time (s)	231
Settling time (s)	822
Overshoot (%)	7.94

(b) Performance parameters

Figure 4.6 depicts the corresponding controller output and the overall thermal behavior of the electrolyzer. Figure 4.6a shows the variation of the PID output signal, ranging from 17.5 $\mathrm{L\,min^{-1}}$ at the electrolyzer's minimum load to 193 $\mathrm{L\,min^{-1}}$ at the nominal load. It is worth noting that the controller's saturation limits are not reached in this scenario. As for the stack temperature profile (Figure 4.6b), it shows an average value of 60 °C, aligning well with $T_\mathrm{stack,set} = 60$ °C, indicating effective stack temperature control for this application. The maximum deviation from the stack set temperature is 0.5 °C. The cooling load (Figure 4.6c) exhibits traits similar to those of the power input curve, as the cooling load is directly proportional to the electrolyzer's power input. The peak cooling load required coincides with the electrolyzer's nominal operation point. Notably,

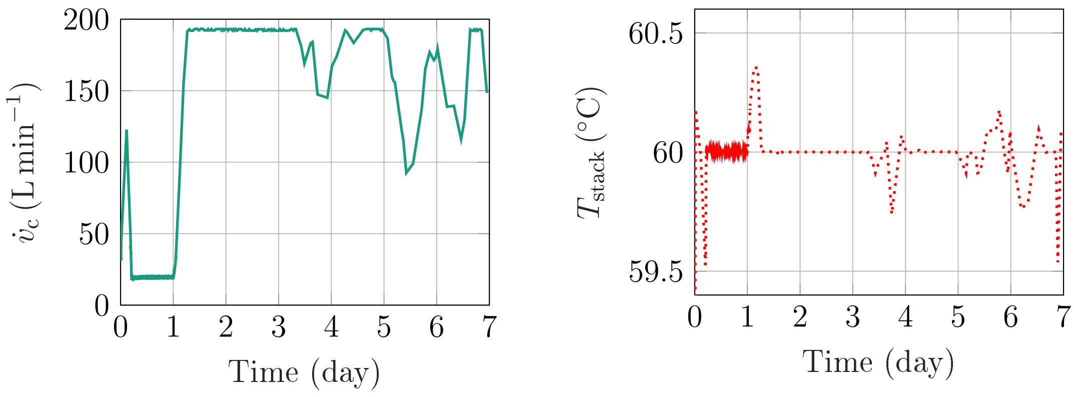

(a) PID controller output

(b) Stack temperature profile

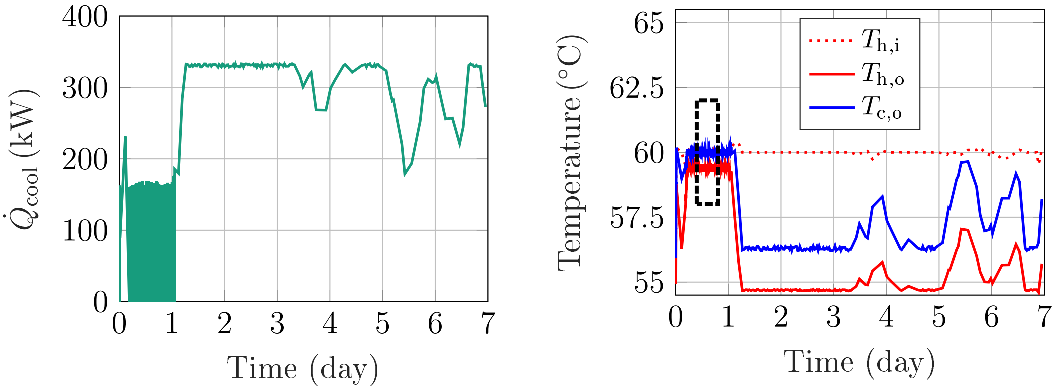

(c) Cooling load profile

(d) PHE temperature profiles

Figure 4.6: Electrolyzer's behavior with PHE FP model and PID Controller 1.

during stack operation at minimum load, the cooling load displays oscillatory behavior from 0 kW to 168 kW suggestive of an intermittent "on-off" switch in the computation of the cooling load. This oscillating behavior can be understood in light of the temperature profiles of the cold fluid outlet and hot fluid inlet streams. Figure 4.6d presents the temperature profiles of the hot and cold fluid, highlighting the region where the $\dot{Q}_{\mathrm{cool}}$ oscillations occur using a dashed rectangle. In this region, the cold fluid outlet and hot fluid inlet temperature profiles get closer, reducing the driving force for the heat transfer process. Further detail of the highlighted region in Figure 4.6d is provided in Figure 4.7 for a suitable time span, illustrating the intermittent cross of the cold fluid outlet and hot fluid inlet temperature profiles. The green markers in Figure 4.7 denote the operating points satisfying $T_{\mathrm{c,o}} > T_{\mathrm{h,i}}$, resulting in $\dot{Q}_{\mathrm{cool}} = 0$ according to the constraint definition for (2.7) and its application in (2.14). Similarly, whenever $T_{\mathrm{c,o}} < T_{\mathrm{h,i}}$, $\dot{Q}_{\mathrm{cool}} \neq 0$.

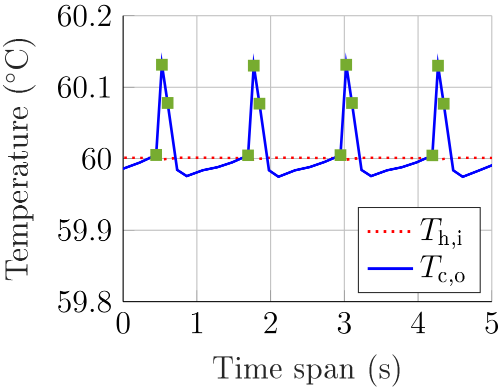

Figure 4.7: Detailed temperature profiles of highlighted region in Figure 4.6d.

4.3.2 Plant with PHE MTI model

For evaluating the plant's performance using the PHE MTI model, Controller 1's parameters are utilized, with the lower saturation limit adjusted to 78 L min^{-1} based on the findings presented in Figure 4.3. The parameters for this PID controller, Controller 2, can be found in Table 4.5. Figure 4.8 provides a visual representation of the controller's output and the overall thermal performance of the electrolyzer.

Table 4.5: Set up and performance parameters of Controller 2

Property	Value
Proportional action, K_p	15.30
Integral action, K_i	0.11
Derivative action, K_d	-117.44
Filter coefficient, N	0.0114
Saturation lower limit (L min^{-1})	78
Saturation upper limit (L min^{-1})	800
Initial value (L min^{-1})	130

(a) Set up parameters

Performance and robustness indicators	Value
Rise time (s)	146
Settling time (s)	1050
Overshoot (%)	26.4

(b) Performance parameters

Figure 4.8a shows the PID controller output varying from 105.4 L min^{-1} to 178.9 L min^{-1} without reaching its saturation limits. The stack temperature profile Figure 4.8b has similar characteristics when compared to Figure 4.6b, showing that the PHE MTI model successfully represents the essential dynamics of the FP model where the maximum deviation of 0.5 °C from the temperature set point in the FP model is not exceeded. The cooling load (Figure 4.8c) presents the same oscillating behavior seen in Figure 4.6c, explained by the cross of temperature profiles in Figure 4.8d and their detailed analysis in Figure 4.7.

The next step in exploring the PID controller tuning involves utilizing the autotuning method of the MATLAB PID tuner app with the plant employing the PHE MTI model. This is fundamental for determining the suitability of the PID autotuning algorithm based

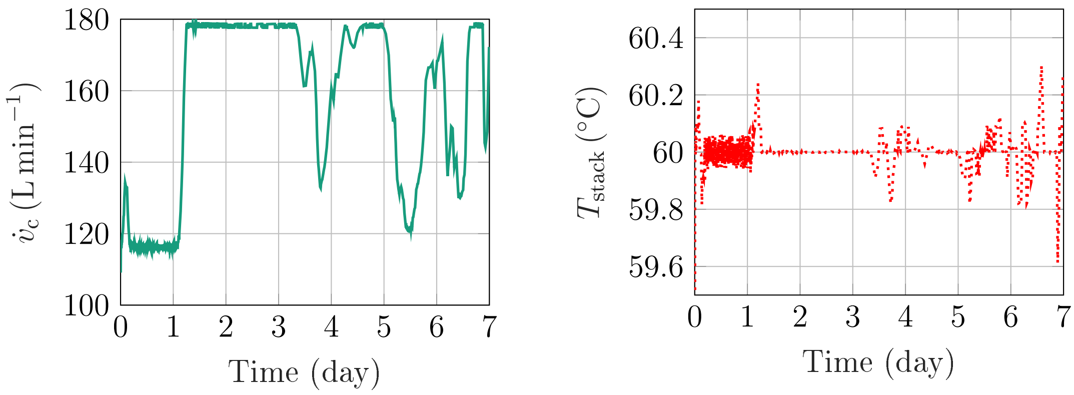

(a) PID controller output

(b) Stack temperature profile

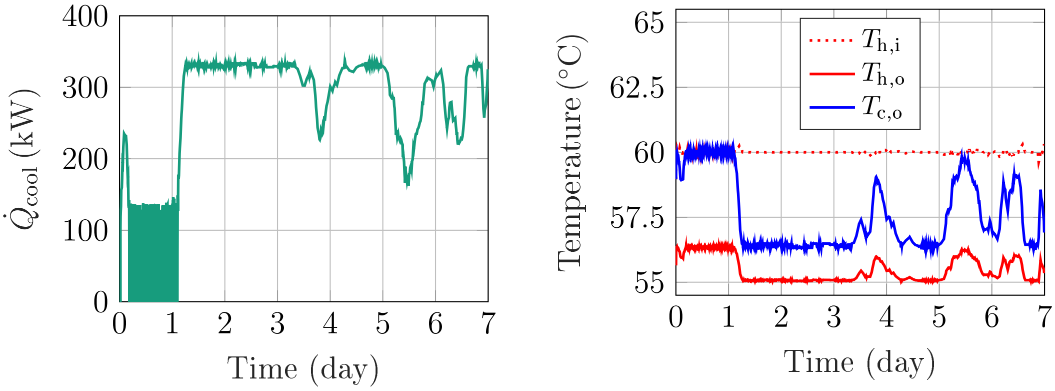

(c) Cooling load profile

(d) PHE temperature profiles

Figure 4.8: Electrolyzer's behavior with PHE MTI model and PID Controller 2.

on the PHE MTI model. Table 4.6 displays the parameters for the autotuned Controller 3. The outcomes indicate that the autotuning approach, based on the PHE MTI model for designing a PID controller, results in slower dynamics compared to Controller 2, with a rise time increase of 561 % and a settling time increase of 225 %. Figure 4.9 illustrates the controller output and PHE temperature profiles, revealing ineffective temperature control due to erratic behavior in predicting PHE outlet temperatures, where $T_{c,o} > T_{h,i}$. This behavior pushes the PID output signal to its upper saturation limit without effectively cooling the system. Hence, it is concluded that the autotune method is not suitable for

Table 4.6: Set up and performance parameters of Controller 3

Property	Value
Proportional action, K_p	2.88
Integral action, K_i	0.00052
Derivative action, K_d	-103.15
Filter coefficient, N	0.00275
Saturation lower limit (L min^{-1})	78
Saturation upper limit (L min^{-1})	800
Initial value (L min^{-1})	130

(a) Set up parameters

Target perfomance parameters	Value
Response time (s)	1250
Transient behavior	0.6
Performance and robustness indicators	
Rise time (s)	966
Settling time (s)	3420
Overshoot (%)	7.94

(b) Performance parameters

tuning the PID controller based on a plant using the PHE MTI model.

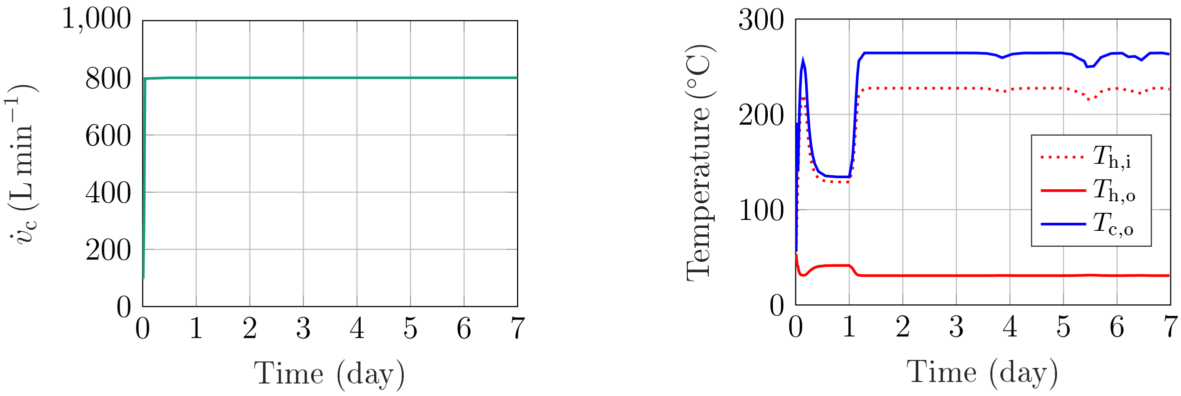

(a) PID controller output (b) PHE temperature profiles

Figure 4.9: Electrolyzer's behavior with PHE MTI model and PID Controller 3.

However, manual tuning of the PID controller using the PHE MTI model is conducted to explore a PID controller with faster dynamics than Controller 3 to achieve adequate temperature control. Table 4.7 displays the parameters for Controller 4, obtained after a trial and error procedure of modifying the target performance parameters. The plant simulation using this PID controller yields results similar to those presented in Figure 4.8. To ensure a fair comparison between the different PID controllers and the corresponding plant simulations, the models' performance is assessed based on their execution time and their temperature control efficiency, measured with the root-mean-square error (RMSE) of the T_{stack} profile in relation to the $T_{\text{stack,set}}$. Table 4.8 displays the metrics for the simulation sets in Simulink, utilizing a device equipped with a 13th-generation Intel Core i7 1.90 GHz processor and 16.0 GB of RAM. These metrics correspond to the PID controllers referenced in Table 4.3.

Table 4.7: Set up and performance parameters of Controller 4.

Property	Value
Proportional action, K_p	36.28
Integral action, K_i	0.1564
Derivative action, K_d	-20.24
Filter coefficient, N	1.793
Saturation lower limit (L min^{-1})	78
Saturation upper limit (L min^{-1})	800
Initial value (L min^{-1})	130

(a) Set up parameters

Target perfomance parameters	Value
Response time (s)	128
Transient behavior	0.558
Performance and robustness indicators	
Rise time (s)	96.6
Settling time (s)	639
Overshoot (%)	10.9

(b) Performance parameters

The results depicted in Figure 4.6 and 4.8 show how the PHE MTI consistently replicates the dynamics of the FP model when used with an appropriate PID controller, such as Controller 2. Table 4.8 demonstrates a significant improvement in computational efficiency, with a 74 % reduction in model execution time compared to using the PHE FP

Table 4.8: PID controllers performance comparison.

ID	Model execution time (s)	RMSE T_{stack} (°C)
Controller 1	61.7	0.16
Controller 2	15.7	0.03
Controller 3	5.5	137
Controller 4	28.9	0.01

model simulated with Controller 1. Furthermore, the PHE MTI model structure facilitates seamless integration with multistack electrolyzer models using MTI structures, such as the one presented in [11].

The results for Controller 3 indicate that the autotuning method of the PID Tuner app is ineffective in achieving proper temperature control, as evidenced by an RMSE of T_{stack} equal to 137 °C and the results shown in Figure 4.9.

Manual tuning enables the configuration of a PID controller that achieves satisfactory temperature control, as demonstrated by Controller 4 with a RMSE for T_{stack} of 0.01 °C and a model execution time of 28.9 s. A comparison of the plant performance using Controller 2 and Controller 4 shows a 66.6 % improvement in the temperature control goal, while increasing the model execution time by 84 %.

Based on these findings, the plant using the PHE MTI model and PID Controller 2 is used to analyze power consumption in BOP pumping components, showcasing the potential for further exploration enabled by the enhanced electrolyzer model in Figure 3.2.

4.4 Pumps power consumption

The assessment of pump power usage relies on the volume flow and pressure drop characteristics of the hot and cold fluids, as defined by (2.54). With regard to volume flow characteristics, Figure 4.10 illustrates a significant contrast in flow rates between the hot and cold circuits, with the flow rate in the hot circuit being 5 to 8 times greater than that in the cold circuit. Table 4.9 presents a summary of the pressure analysis for power consumption calculation, considering the individual and total pressure drop characteristics as stipulated in (2.55).

Upon reviewing the pressure drop in the hot fluid circuit, it is evident that it is approximately six times higher than the pressure drop in the cold circuit. In the cold water circuit, the air cooler has the most significant impact on the pressure drop, contributing to 56 % of the total pressure drop in the circuit. For the hot circuit, the PHE contributes 59 % to the total pressure drop, while the stack accounts for 37 %. The power consumption of the pumps is detailed in Figure 4.11. According to Figure 4.11a, the feed water pump requires on average 97 % of the total power consumption associated with running the

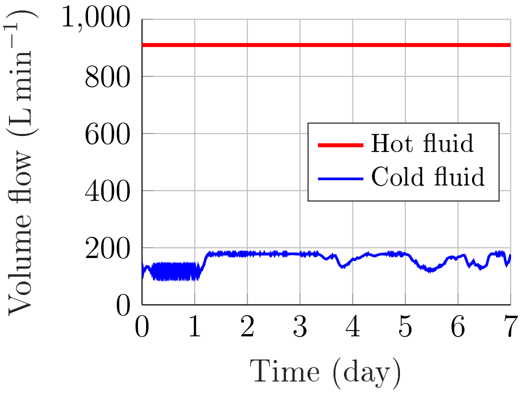

Figure 4.10: Volume flow profiles of hot and cold fluid.

Table 4.9: Pressure drop summary for hot and cold fluid circuits.

	Hot circuit	Cold circuit
Fluid	Feed water	Cooling water
Mean pressure drop (kPa)	540	79
Other equipment	Stack	Air cooler
Pressure drop distribution		
Piping network	4.0 %	26.0 %
Plate heat exchanger	59.0 %	18.0 %
Other equipment	37.0 %	56.0 %

feed water and cooling circuits in the PEM electrolyzer. This high consumption is primarily due to the excessive feed water flow required for the stack (Figure 4.10) and the pressure drop distribution in the components of the circuits (Table 4.9), indicating the potential for power optimization strategies related to the operation of the hot circuit or the selection of a more hydraulic-efficient PHE geometry and internal configuration of the stack. The analysis indicates that optimizing the operation of the equipment in the cold fluid circuit is not the critical path leading to a significant reduction in power consumption for the BOP pumping components. Figure 4.11b summarizes the total pump power consumption ranging between 10.34 kW and 10.65 kW. For the assessment of power distribution between the pumping BOP components and the the total power consumption of the electrolyzer (stack plus pumping BOP components), the BOP power allocation factor is calculated using

$$\gamma = \frac{(\dot{W}_{\mathrm{pump,h}} + \dot{W}_{\mathrm{pump,c}})}{(\dot{W}_{\mathrm{pump,h}} + \dot{W}_{\mathrm{pump,c}}) + \mathcal{P}_{stack}} \times 100. \tag{4.1}$$

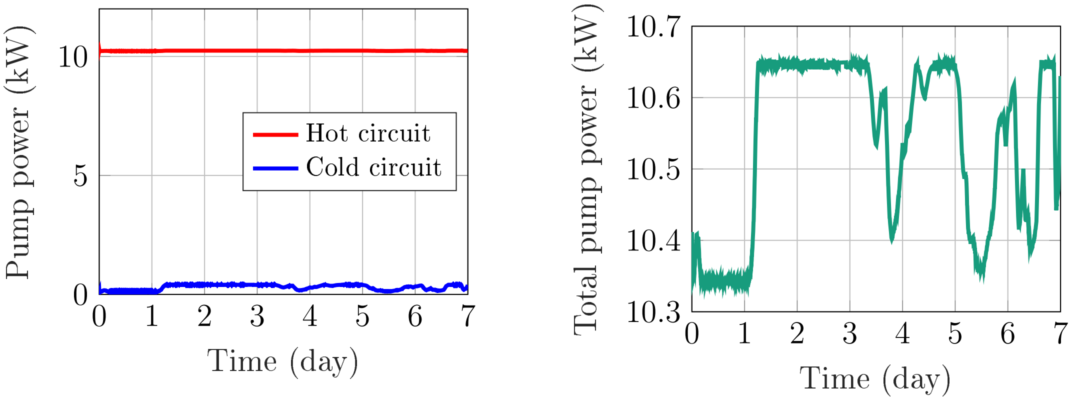

(a) Individual pump power consumption

(b) Total pumps power comsumption

Figure 4.11: Pumps power consumption profiles.

This factor reveals that running the pumps for the cooling system accounts for a power consumption between 1.0 % and 5.4 % of the electrolyzer's total power usage (Figure 4.12).

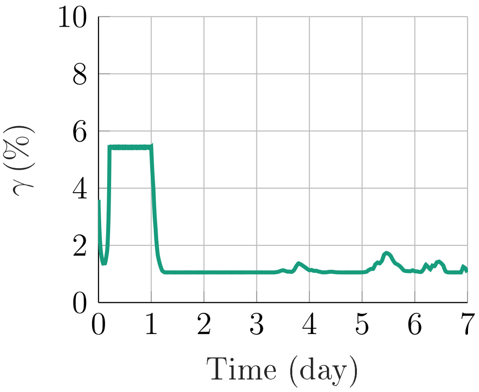

Figure 4.12: Pumps power consumption allocation.

5 Conclusion

In this chapter, a summary provides a concise overview of the methodology employed and highlights the key findings in this thesis. Additionally, it presents an outlook section that delineates potential extensions of the current study and proposes areas for future research exploration.

5.1 Summary

This thesis has explored the critical role of effective temperature control at the stack in a proton exchange membrane water electrolysis (PEMWE) system, which is essential for the long-term reliability and efficiency of green hydrogen production. Through the utilization of an existing thermal model for a 1MW proton exchange membrane (PEM) electrolyzer as a basis, an enhanced model incorporating the cooling system for this electrolyzer was developed using MATLAB and SIMULINK. In this regard, a plate heat exchanger (PHE) predicated on first principles (FP) modeling was dimensioned, demonstrating the potential of PHEs in achieving a high thermal effectiveness of 86% for this application. The incorporation of a simplified version of the FP model in the electrolyzer cooling system involved testing linear time-invariant (LTI) and multilinear time-invariant (MTI) modeling approaches under variable stack power input conditions. Multiple simulations demonstrated that the PHE MTI model successfully represents the dynamics of the FP model, consistently outperforming traditional LTI models. Moreover, the integration of the PHE MTI with the stack's model resulted in a remarkable reduction in computation time by 74 % in comparison to the FP model, thereby highlighting the practical advantages of the MTI approach in promoting faster and more efficient simulations without compromising accuracy for large-scale simulations of cooling system in PEM electrolyzers.

When paired with a suitable PID controller, both the PHE MTI and FP models effectively maintained the feed water temperature within the set reference of 60°C. This showcases the robustness of the control strategy employed, avoiding temperature runaways in the stack and thereby extending its operational lifespan.

In the context of PID controller tuning, it was found that while the autotuning algorithm available in the MATLAB PID Tuner app is suitable for tuning the electrolyzer's

PID controller using the PHE FP model, it is unsuitable for tuning using the PHE MTI model. This difference highlights the need for tailored tuning approaches depending on the specific model employed, shedding light on the limitations of the autotuning algorithm in handling the MTI model.

Additionally, the structure of the implemented model enabled the estimation and breakdown of power consumption associated with the balance of plant (BOP) pumping components in the electrolyzer's feed water and cooling water systems. The analysis revealed that the feed water pump accounts for a substantial 97 % of the total power consumption related to the operation of the feed water and cooling water circuits. The most significant pressure drops in the feed water circuit occur at the PHE and the cell stack, which together account for 96 % of the total pressure drop. This finding underscores the potential for power optimization strategies through operational adjustments or selecting more hydraulic-efficient components for the hot fluid circuit. Conversely, optimizing the cooling water circuit presents a minor opportunity for significantly reducing the total pump power consumption. Overall, running the pumps in the feed water and cooling water circuits constitutes between 1 % and 5.4 % of the total power consumption of the electrolyzer, including both the stack and the cooling water system.

5.2 Outlook

Building on these findings, several future research directions are proposed to enhance the performance and applicability of the PEM electrolyzer model consolidated in this thesis. Firstly, incorporating variable feed water flow can unlock new power optimization strategies within PEMWE cooling systems, leading to more efficient energy use and adapting to varying stack power input. Extending the cooling system model to include the power consumption of the air cooler will increase the accuracy of power consumption predictions, providing a more detailed understanding of the entire system's energy dynamics. Moreover, designing strategies for the effective use of waste heat released from the cooling system can further improve the energy matrix of PEMWE systems. Exploring these strategies can contribute to energy conservation and cost reduction, for example, by coupling the cooling water system with preheating stages for feed water desalination. In this regard, future research should also address the incorporation of additional BOP systems into this model, such as water desalination and hydrogen conditioning, to improve the total power consumption assessment and provide a complete picture of the system's energy requirements.

Considering the extension to implicit MTI models can help capture non-linear hybrid dynamics, such as saturations, which the current explicit PHE MTI model does not fully address. This will enhance the robustness of the PHE thermal response. Regarding the controller, the structure of the current PID controller, based on MATLAB linearization of the non-linear model, can be further explored using multilinear models to improve tunable PID parameters, potentially yielding more effective control strategies. Additionally, model predictive control (MPC) strategies for direct optimization or using the MTI model for successive linearization can lead to more efficient and accurate control schemes. This research direction holds promise for improving operational efficiency and system responsiveness.

Bibliography

[1] Umweltbundesamt. *Nationaler Inventarbericht zum Deutschen Treibhausgasinventar 1990 - 2020: Submission under the United Nations framework convention on climate change and the kyoto protocol 2022*. 2022. URL: https://www.umweltbundesamt.de/sites/default/files/medien/1410/publikationen/2022-05-31_climate-change_25-2022_nir-2022_en.pdf (visited on 03/21/2024).

[2] Umweltbundesamt. *Energy target 2050: 100% renewable electricity supply*. 2010. URL: https://www.umweltbundesamt.de/sites/default/files/medien/378/publikationen/energieziel_2050_kurz.pdf (visited on 03/21/2024).

[3] P. Denholm. “Energy storage to reduce renewable energy curtailment.” In: *IEEE Power and Energy Society General Meeting* (2012), pp. 1–4. DOI: 10.1109/PESGM.2012.6345450.

[4] C. Rakousky et al. “Polymer electrolyte membrane water electrolysis: Restraining degradation in the presence of fluctuating power.” In: *Journal of Power Sources* 342 (2017), pp. 38–47. ISSN: 03787753. DOI: 10.1016/j.jpowsour.2016.11.118. URL: https://www.sciencedirect.com/science/article/pii/S0378775316316858.

[5] S. H. Frensch. *Lifetime Investigation of PEM Electrolyzers under Realistic Load Profiles*. 2018. DOI: 10.54337/aau300037423.

[6] V. Liso et al. “Modelling and Experimental Analysis of a Polymer Electrolyte Membrane Water Electrolysis Cell at Different Operating Temperatures.” In: *Energies* 11.12 (2018), p. 3273. DOI: 10.3390/en11123273.

[7] M. Chandesris et al. “Membrane degradation in PEM water electrolyzer: Numerical modeling and experimental evidence of the influence of temperature and current density.” In: *International Journal of Hydrogen Energy* 40.3 (2015), pp. 1353–1366. ISSN: 03603199. DOI: 10.1016/j.ijhydene.2014.11.111.

[8] P. Olivier et al. “Low-temperature electrolysis system modelling: A review.” In: *Renewable and Sustainable Energy Reviews* 78 (2017), pp. 280–300. ISSN: 13640321. DOI: 10.1016/j.rser.2017.03.099.

[9] M. Espinosa-López et al. “Modelling and experimental validation of a 46 kW PEM high pressure water electrolyzer.” In: *Renewable Energy* 119 (2018), pp. 160–173. ISSN: 09601481. DOI: 10.1016/j.renene.2017.11.081.

[10] M. Rizwan et al. “Design considerations for industrial water electrolyzer plants.” In: *International Journal of Hydrogen Energy* 46.75 (2021), pp. 37120–37136. ISSN: 03603199. DOI: 10.1016/j.ijhydene.2021.09.018.

[11] A. Luxa et al. “Multilinear Modeling and Simulation of a Multi-stack PEM Electrolyzer with Degradation for Control Concept Comparison.” In: *Proceedings of the 12th International Conference on Simulation and Modeling Methodologies, Technologies and Applications*. SCITEPRESS - Science and Technology Publications, 2022, pp. 52–62. ISBN: 978-989-758-578-4. DOI: 10.5220/0011263300003274.

[12] E. Amores et al. “Development of an operation strategy for hydrogen production using solar PV energy based on fluid dynamic aspects.” In: *Open Engineering* 7.1 (2017), pp. 141–152. DOI: 10.1515/eng-2017-0020.

[13] Nel Hydrogen. *PEM Electrolyser - M Series | Nel Hydrogen*. 2018. URL: https://nelhydrogen.com/product/m-series-electrolyser/ (visited on 02/22/2024).

[14] Nel Hydrogen. *PEM Electrolyser - MC Series | Nel Hydrogen*. 2019. URL: https://nelhydrogen.com/product/mc-series-electrolyser/ (visited on 02/22/2024).

[15] Teledyne Energy Systems. *Titan EL Series - Dual Module: On-site hydrogen generation system*. 2019. URL: https://www.teledynees.com/en-us/Hydrogen_/Documents/EL%20Dual%20Mod%20Spec%20Sheet.pdf (visited on 02/22/2024).

[16] Plug Power Inc. *The Plug EX-425D: Best in-class PEM electrolysis based on nearly 50 years of experience*. URL: https://www.plugpower.com/wp-content/uploads/2022/04/EX-425D_042522.pdf (visited on 02/22/2024).

[17] L. Wang, B. Sundén, R.M. Manglik. *Thermal-hydraulic analysis of plate-and-frame heat exchangers*. Southampton: WIT, 2002. ISBN: 978-1-85312-737-3.

[18] S. Kakaç et al. *Heat Exchangers: Selection, Rating, and Thermal Design*. 3rd edition. EBL-Schweitzer. Hoboken: CRC Press, 2012. ISBN: 978-1-4398-4991-0.

[19] L. Pekař. “Introduction to heat exchangers.” In: *Advanced Analytic and Control Techniques for Thermal Systems with Heat Exchangers*. Ed. by Libor Pekař. Academic Press, 2020, pp. 3–20. ISBN: 978-0-12-819422-5. DOI: 10.1016/B978-0-12-819422-5.00001-3. URL: https://www.sciencedirect.com/science/article/pii/B9780128194225000013.

[20] R. K. Shah et al. “Heat exchanger basic thermal design methods.” In: *Handbook of Heat Transfer Applications* 2 (1985).

[21] H-TEC Systems. *PEM-Elektrolyseur ME450 Datenblatt*. URL: https://www.h-tec.com/fileadmin/user_upload/produkte/produktseiten/ME450-1400/spec-sheet/H-TEC-Datenblatt-ME450-DE-23-08.pdf (visited on 02/22/2024).

[22] J. Saari. *Heat Exchanger Dimensioning*. 2010.

[23] R. K. Shah et al. *Fundamentals of heat exchanger design.* Hoboken NJ: John Wiley & Sons, 2003. ISBN: 0-471-32171-0.

[24] R. K. Shah et al. “Heat Exchangers, 2. Heat Transfer for Heat Exchanger Design.” In: *Ullmann’s Encyclopedia of Industrial Chemistry.* Wiley, 2003, pp. 1–61. ISBN: 9783527303854. DOI: 10.1002/14356007.t12{\textunderscore}t01.

[25] Alfa Laval. *The theory behind heat transfer: Plate heat exchangers.* Ed. by Alfa Laval. 2004. URL: www.alfalaval.com (visited on 02/15/2024).

[26] H. Kumar. “The Plate Heat Exchanger: Construction and Design.” In: *First U.K. National Conference on Heat Transfer.* Ed. by H. C. Simpson et al. The Institution of Chemical Engineers Symposium Series. Pergamon, 1984, pp. 1275–1288. DOI: 10.1016/B978-0-85295-175-0.50054-0. URL: https://www.sciencedirect.com/science/article/pii/B9780852951750500540.

[27] Don W. Green et al., eds. *Perry’s chemical engineers’ handbook.* Ninth edition, 85th anniversary edition. New York: McGraw Hill Education, 2019. ISBN: 0071834087.

[28] *Ullmann’s Encyclopedia of Industrial Chemistry.* Wiley, 2003. ISBN: 9783527303854. DOI: 10.1002/14356007.

[29] Alfa Laval. *Compact heat exchangers.* 2024-05-31. URL: https://www.alfalaval.com/microsites/increase-efficiency/products/compact-heat-exchangers/ (visited on 05/31/2024).

[30] S. M. Walas. *Chemical process equipment: Selection and design.* 3rd edition. IChemE. 2012. ISBN: 978-0-12-396959-0.

[31] A. Chan et al. “Coolant Considerations for Liquid-Cooling.” In: *2023 39th Semiconductor Thermal Measurement, Modeling & Management Symposium* (2023), pp. 1–5. DOI: 10.23919/SEMI-THERM59981.2023.10267902.

[32] Verein Deutscher Ingenieure et al. *VDI-Wärmeatlas.* Berlin, Heidelberg: Springer Berlin Heidelberg, 2013. ISBN: 978-3-642-19980-6. DOI: 10.1007/978-3-642-19981-3.

[33] G. Pangalos. *Model-based Controller Design Methods for Heating Systems.* 2. Auflage. Berlin: Neopubli, 2016. ISBN: 978-3-7418-2306-0.

[34] R. C. Dorf et al. *Modern Control Systems.* 13th edition. Boston: Pearson, 2016. ISBN: 9780134407623. (Visited on 05/29/2024).

[35] G. Pangalos et al. “Tensor Systems - Multilinear Modeling and Applications.” In: *Proceedings of the 3rd International Conference on Simulation and Modeling Methodologies, Technologies and Applications.* SciTePress - Science and and Technology Publications, 2013, pp. 275–285. ISBN: 978-989-8565-69-3. DOI: 10.5220/0004475602750285.

[36] K. Kruppa et al. “Multilinear Approximation of Nonlinear State Space Models.” In: *IFAC Proceedings Volumes* 47.3 (2014), pp. 9474–9479. ISSN: 1474-6670. DOI: 10.3182/20140824-6-ZA-1003.00455.

[37] R. P. Borase et al. “A review of PID control, tuning methods and applications.” In: *International Journal of Dynamics and Control* 9.2 (2021), pp. 818–827. ISSN: 2195-2698. DOI: 10.1007/s40435-020-00665-4. URL: https://link.springer.com/article/10.1007/s40435-020-00665-4.

[38] Y. Li et al. “PID control system analysis and design.” In: *IEEE Control Systems Magazine* 26.1 (2006), pp. 32–41. ISSN: 0272-1708. DOI: 10.1109/MCS.2006.1580152.

[39] Y. A. Çengel et al. *Fluid Mechanics: Fundamentals and Applications.* McGraw-Hill series in mechanical engineering. McGraw-HillHigher Education, 2006. ISBN: 9780073044651.

[40] J. A. Roberson et al. *Engineering Fluid Mechanics.* Twelfth edition. Place of publication not identified: JOHN WILEY, 2019. ISBN: 9781119723509.

[41] M. J. Kaiser et al. *Pipeline Rules of Thumb Handbook: A Manual of Quick, Accurate Solutions to Everyday Pipeline Engineering Problems.* Elsevier Science, 2022. ISBN: 9780128227893. URL: https://books.google.de/books?id=cRExEAAAQBAJ.

[42] G. S. Brown. “How to predict pressure drop before designing the piping.” In: *Chemical engineering (New York, NY)* 94.4 (1987), pp. 85–86.

[43] American Petroleum Institute. “API RP14E: Recommended practice for design and installation of offshore production platform piping systems.” In: 5 (2013).

[44] L. Ai Li. *Piping fluid flow material selection and line sizing: Engineering design guideline.* 2007.

[45] A. S. Tijani et al. “Computational Modelling of the Flow Field of An Electrolyzer System using CFD.” In: *Energy Procedia* 79 (2015), pp. 195–203. ISSN: 18766102. DOI: 10.1016/j.egypro.2015.11.462. (Visited on 05/23/2024).

[46] S. Toghyani et al. “Thermal and electrochemical analysis of different flow field patterns in a PEM electrolyzer.” In: *Electrochimica Acta* 267 (2018), pp. 234–245. ISSN: 00134686. DOI: 10.1016/j.electacta.2018.02.078. (Visited on 05/23/2024).

[47] H. Ito et al. “Effect of flow regime of circulating water on a proton exchange membrane electrolyzer.” In: *International Journal of Hydrogen Energy* 35.18 (2010), pp. 9550–9560. ISSN: 03603199. DOI: 10.1016/j.ijhydene.2010.06.103.

[48] N. Briguglio et al. “Design and testing of a compact PEM electrolyzer system.” In: *International Journal of Hydrogen Energy* 38.26 (2013), pp. 11519–11529. ISSN: 03603199. DOI: 10.1016/j.ijhydene.2013.04.091.

[49] Hudson Products Corporation. *The basics of air-cooled heat exchangers*. 2007. URL: http://www.hudsonproducts.com.

[50] J. R. Couper et al. *Chemical Process Equipment: Selection and Design*. Elsevier Science, 2005. ISBN: 9780080476476. URL: https://books.google.lu/books?id=xFkLuxL115AC.

[51] G. Lichtenberg. *MTI Toolbox 1.0*. 2017. URL: https://www.ls.haw-hamburg.de/~observe/?page_id=345.

[52] C. Piazzola et al. “Algorithm 1040: The Sparse Grids Matlab Kit - a Matlab implementation of sparse grids for high-dimensional function approximation and uncertainty quantification.” In: *ACM Transactions on Mathematical Software* 50.1 (2024). DOI: 10.1145/3630023.

A Appendix

A.1 Fluid properties sensitivity analysis

For the temperature-dependent fluid properties required for the energy balances, a sensitivity analysis is carried out for the operating intervals defined in subsection 3.4.2. Here, the relevant properties are calculated at the upper and lower boundaries of the temperature intervals, and the variation with respect to their value at mean temperature is reported. For the analysis, the density and specific heat are explicitly considered. The variation of viscosity and thermal conductivity is considered through the computation of the overall heat transfer coefficient as shown in (2.8)and (2.28). The temperature interval for the hot and cold fluids corresponds to $T_{\mathrm{h}} \in [50\ ^{\circ}\mathrm{C},\ 65\ ^{\circ}\mathrm{C}]$ and $T_{\mathrm{c}} \in [25\ ^{\circ}\mathrm{C},\ 60\ ^{\circ}\mathrm{C}]$, respectively. Figure A.1 presents the variation of the density and the specific heat capacity in these intervals.

Table A.1 summarizes the deviation of fluid properties in the designated temperature intervals, showing their maximum variation from the mean temperature value to the upper or lower temperature of the interval. For the hot fluid, this variation corresponds to 0.07 % for the specific heat capacity and 0.4 % for the density. This variation for the cold fluid is higher, being 1.3 % for the specific heat capacity and 1.1 % for the density. These low variations in the designated temperature interval suggest that the model could be simplified by considering constant average values for the fluid properties.

For this analysis, a reference case at state state is simulated considering the properties c_p, ρ and U as temperature-dependent properties in a heat exchanger with the configuration presented in Table 4.1 using the plate geometry presented in Table 3.3.

Table A.1: Sensitivity analysis of selected fluid properties.

		Property value			Property variation between	
Fluid	Property	at T_{low}	at T_{m}	at T_{high}	$[T_{\mathrm{low}}, T_{\mathrm{high}}]$	$\max(\{[T_{\mathrm{low}}, T_{\mathrm{m}}], [T_{\mathrm{m}}, T_{\mathrm{high}}]\})$
Hot	c_p ($\mathrm{J\,kg^{-1}\,K^{-1}}$)	4178	4181	4184	0.12 %	0.07 %
	ρ ($\mathrm{kg\,m^{-3}}$)	986	982	978	0.8 %	0.4 %
Cold	c_p ($\mathrm{J\,kg^{-1}\,K^{-1}}$)	3781	3828	3879	2.57 %	1.30 %
	ρ ($\mathrm{kg\,m^{-3}}$)	1034	1024	1012	2.1 %	1.1 %

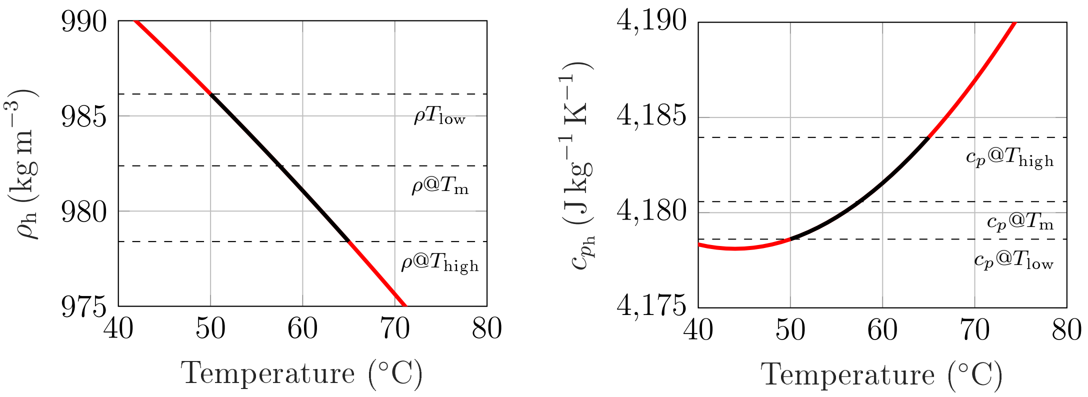

(a) Feed water density

(b) Feed water specific heat capacity

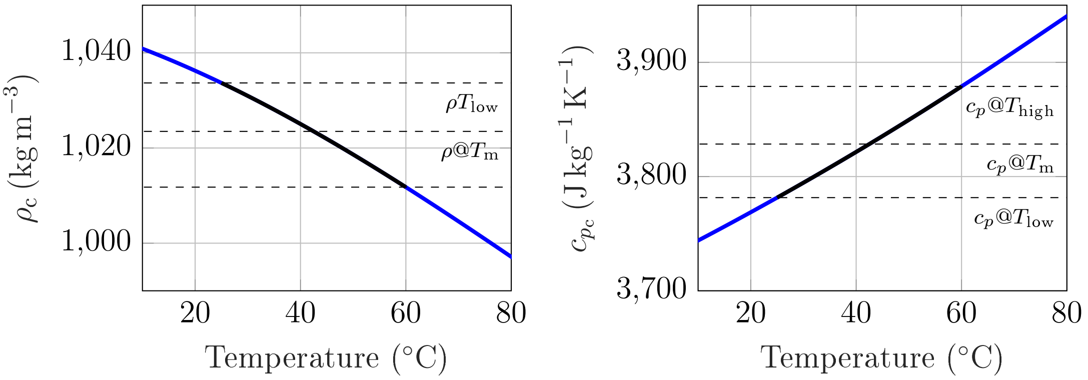

(c) Cooling water density

(d) Cooling water specific heat

Figure A.1: Sensitivity analysis of fluid properties.

The results of this reference case are presented in Table A.2 as a benchmark for later comparison.

Table A.2: Steady-state condition of reference case of study.

Property	Hot fluid	Cold fluid
Name	Feed water	Cooling water
Mass flow (kg s^{-1})	14.9	3.4
Inlet temperature (°C)	60	30
Outlet temperature (°C)	54.5	55.9
Fouling resistance (m^2 K W^{-1})	0.5×10^{-4}	0

Based on these simulated outlet temperatures (Table A.2), the corresponding average properties are calculated at mean tempetarure and summarized in Table A.3.

Table A.3: Average fluid properties calculated for reference case of study.

Averaged property	Hot fluid	Cold fluid
Specific heat capacity ($\mathrm{J\,kg^{-1}\,K^{-1}}$)	4180.5	3828.5
Density ($\mathrm{kg\,m^{-3}}$)	982.5	1023.5
Overall heat transfer coefficient ($\mathrm{W\,m^{-2}\,K^{-1}}$)	4000	

The sensitivity analysis is carried out by simulating the heat transfer process based on two scenarios: one computed by recalculating the temperature-dependent properties and the other using average constant values for these properties. Table A.4 presents the computed outlet temperatures and relative errors of the scenarios simulated. The relative error using average properties was not higher than 0.1 % , proving this approach suitable for computing the PHE outlet temperatures in this PEM electrolysis application.

Table A.4: Calculated error for PHE outlet temperatures.

Scenario	$T_{\mathrm{h,o}}$ (°C)	$T_{\mathrm{c,o}}$ (°C)	$T_{\mathrm{h,o}}$ error (%)	$T_{\mathrm{c,o}}$ error (%)
c_p, ρ and U: Temperature dependent	54.51	55.92	-	-
c_p, ρ and U: Average values	54.52	55.90	0.01 %	0.03 %